Molecular Mechanism for the Self-supported Synthesis of Graphitic Carbon Nitride from Urea Pyrolysis

Mukhopadhyay, Titas Kumar; Leherte, Laurence; Datta, Ayan

Published in:
The Journal of Physical Chemistry Letters

DOI:
10.1021/acs.jpclett.0c03559

Publication date:
2021

Document Version
Peer reviewed version

Molecular Mechanism for the Self-supported Synthesis of Graphitic Carbon Nitride from Urea Pyrolysis

Titas Kumar Mukhopadhyay[a], Laurence Leherte[b]*, Ayan Datta[a]*

[a]School of Chemical Sciences, Indian Association for the Cultivation of Science, 2A and 2B Raja S.C.Mullick Road, Jadavpur, Kolkata-700032, West Bengal, India.

[b]Unit of Theoretical and Structural Physical Chemistry, Namur Institute of Structured Matter (NISM), Namur Research Institute for Life Sciences (NARILIS), Namur Medicine & Drug Innovation Center (NAMEDIC), Department of Chemistry, Laboratory of Structural Biological Chemistry, University of Namur, Rue de Bruxelles 61, B-5000 Namur (Belgium)

Abstract:

Quantum chemical calculations combined with Kinetic Monte Carlo simulations are performed to decipher the kinetics for the one-pot synthesis of two-dimensional graphitic carbon nitride (g-C_3N_4) from urea pyrolysis. Two mechanisms are considered, one involving ammelide as the intermediate compound while the other considering cyanuric acid. Different grid growing patterns are investigated, and the size, shape and density of the grids as well as the number and position of the defects are evaluated. We find that, the mechanistic pathway involving ammelide is preferred. Larger *g*-C_3N_4 grids with lower density are achieved when the rate constant for melon growing is inversely proportional to the number of local reaction sites while nearly filled smaller grids are obtained in the opposite scenario. Larger defects appear at the grid periphery while smaller holes appear throughout the grid. The synthesis of extended *g*-C_3N_4 structures is favoured if the *g*-C_3N_4 growing propensity is directly proportional to the number of reaction sites.

TOC Graphic

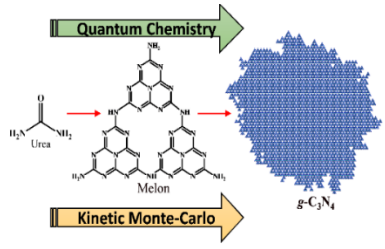

In recent years, Graphitic carbon nitride (g-C_3N_4), a two dimensional, polymeric, π-conjugated, nitrogen-rich semiconductor material has gathered profound interest of the contemporary material research community owing to its high surface area, remarkable thermal and photochemical stability, a medium band-gap of 1.27 eV in conjunction with remarkable properties towards photocatalysis, visible light response, sunlight harvesting, redox catalysis, and recyclable adsorption among many others.[1-5] These intriguing properties of g-C_3N_4 have led to its plausible applications in the realms of metal-free photocatalysis, electrocatalysis, photo sensing, photovoltaics, nanoscale electronic devices, biomedicine, pollutant decontamination, and energy conservation.[4-12] However, widespread applications of g-C_3N_4 demand efficient and highly scalable synthetic roots. In recent years, several studies have been dedicated to the synthesis of g-C_3N_4. It has been suggested that g-C_3N_4 may be prepared via high-pressure, high-temperature routes, solvothermal processes and even using detonative synthetic methodologies. For instance, Antonietti and co-workers performed thermal polycondensation of cyanamide or dicyanamide into g-C_3N_4 under constant N_2 flow in presence of mesoporous host matrices and hard templates.[13-15] Zou et al. demonstrated that direct heating of melamine in a closed system is capable of producing g-C_3N_4.[16] Several researchers found that the thermal transformation of guanylurea dicyanamide can produce g-C_3N_4 and the isocyanic acid produced during this transformation is able to render various organic compounds which, in turn, act as suitable precursors for the synthesis of g-C_3N_4.[17-19] Other precursors commonly used for the generation of g-C_3N_4 are nitrogen-rich, reactive, oxygen-deficient, or oxygen-free compounds comprising of pre-bonded C-N core structures such as cyanamide or dicyanamide, triazine or heptazine derivatives among others.[19-25] However, some of these precursor materials are toxic (such as cyanamide or dicyanamide) to both humans and the environment, some are unstable and few of them are either costly or difficult to synthesize on a significantly large scale.[18, 26-30] Therefore, there has been an urge

for simpler synthetic roots involving low-cost starting materials, reagents, and moderate reaction conditions. In this regard, several research groups have synthesized *g*-C_3N_4 on a large scale from the pyrolysis of urea, both with an additive assistance or in a self-supported atmosphere.[19, 31, 32]

In spite of such progress in developing various preparatory routes for *g*-C_3N_4, the underlying kinetics, to a large extent, remains elusive. Since the majority of reactions yielding *g*-C_3N_4 are multi-step and involve several intermediate products before reaching g-C_3N_4, therefore, the fundamental understanding of the involved molecular events, the associated kinetics of formation, decomposition and decay as well as the kinetic competition of the reactions remains a challenge to better-understand the state-of-the-art synthetic protocols and to introduce proper modifications. While experimental approaches may be endeavoured to venture into this aspect, however, they often suffer from inadequacy to provide exact kinetic data for all intermediate products formed during the consecutive and parallel chemical reactions. Alternatively, "in-silico" approaches are able to model such events with great details and depending on the varying initial conditions, they offer specific predictions to contemplate future modifications of such reactions. One of such approaches dealing particularly with the kinetic aspects of chemical reactions is the Kinetic Monte Carlo (KMC) modelling of coupled chemical reactions proposed by Gillespie.[33, 34] In this method, rather than solving the differential equations that characterize each elementary step involved in the time-dependent composition of a reaction medium, the kinetics is simulated through a set of random processes whose propensity is related to their corresponding rate constants. Working with KMC-based algorithms is thus a convenient way to test reaction mechanisms and kinetic parameters while preserving the stochastic nature of chemical reactions. KMC techniques have been recently applied to a variety of chemical systems such as gas phase reactions, photovoltaic devices, electrochemical systems, crystallization, dissolution rates, and growth of 2D or 3D materials

such as zeolites, and covalent organic frameworks.[35-41]In dealing with chemical reaction kinetics, the activation energies and rate constant parameters are usually obtained from Transition State Theory (TST) using quantum chemistry calculations. Alternatively, these parameters can also be adjusted through comparisons of net rates with experimental values.[42] In the past few decades, several computational studies have been carried out to investigate the structure, stability, stacking patterns, and electronic properties of different polymorphs of *g*-C_3N_4 and different precursor molecules.[43-46] Also, a plethora of computational studies are dedicated to the evaluation of the photocatalytic activity of *g*-C_3N_4 in pure as well as doped forms, however, none of them sheds light into the kinetic aspects for the formation of *g*-C_3N_4, identifying the bottlenecks for the involved series of reactions.[47-49] In this article, we employ detailed quantum chemical calculations in order to investigate the mechanism for the synthesis of *g*-C_3N_4 through the all-inclusive and self-supported pyrolysis of urea at high temperature. The thermodynamic and kinetic data obtained from the electronic structure calculations are further used to illustrate, as a proof of concept, the synthesis of *g*-C_3N_4 monolayers using a Kinetic Monte Carlo (KMC) algorithm and to simultaneously investigate the reaction kinetics and the nature of 2D materials produced during the reaction chain.

g-C_3N_4 may be prepared from a variety of starting materials and using different methodologies, as stated earlier. However, for the present purpose, we have chosen the self-supported reaction scheme, as proposed in reference 31. In this method, urea is utilized as a single-source molecular precursor and it undergoes pyrolysis at a temperature range of 500-550 ºC without any additive assistance. Ammonia is the product of different reaction steps and is further used as a reactant in other steps, thereby making the scheme partly self-supported (Scheme 1).

The current version of the KMC program is based on the modelling of homogeneous chemical reactions according to the formalism developed by Gillespie.[33, 34]To reduce the search

space, the building of graphitic C_3N_4 monolayers is achieved through the progressive filling of grid cells using building blocks, or molecular templates, and packing modes.[41] All lattice cells are defined as active or inactive, i.e., either they are considered as possible growing sites for a monomer molecule or not.

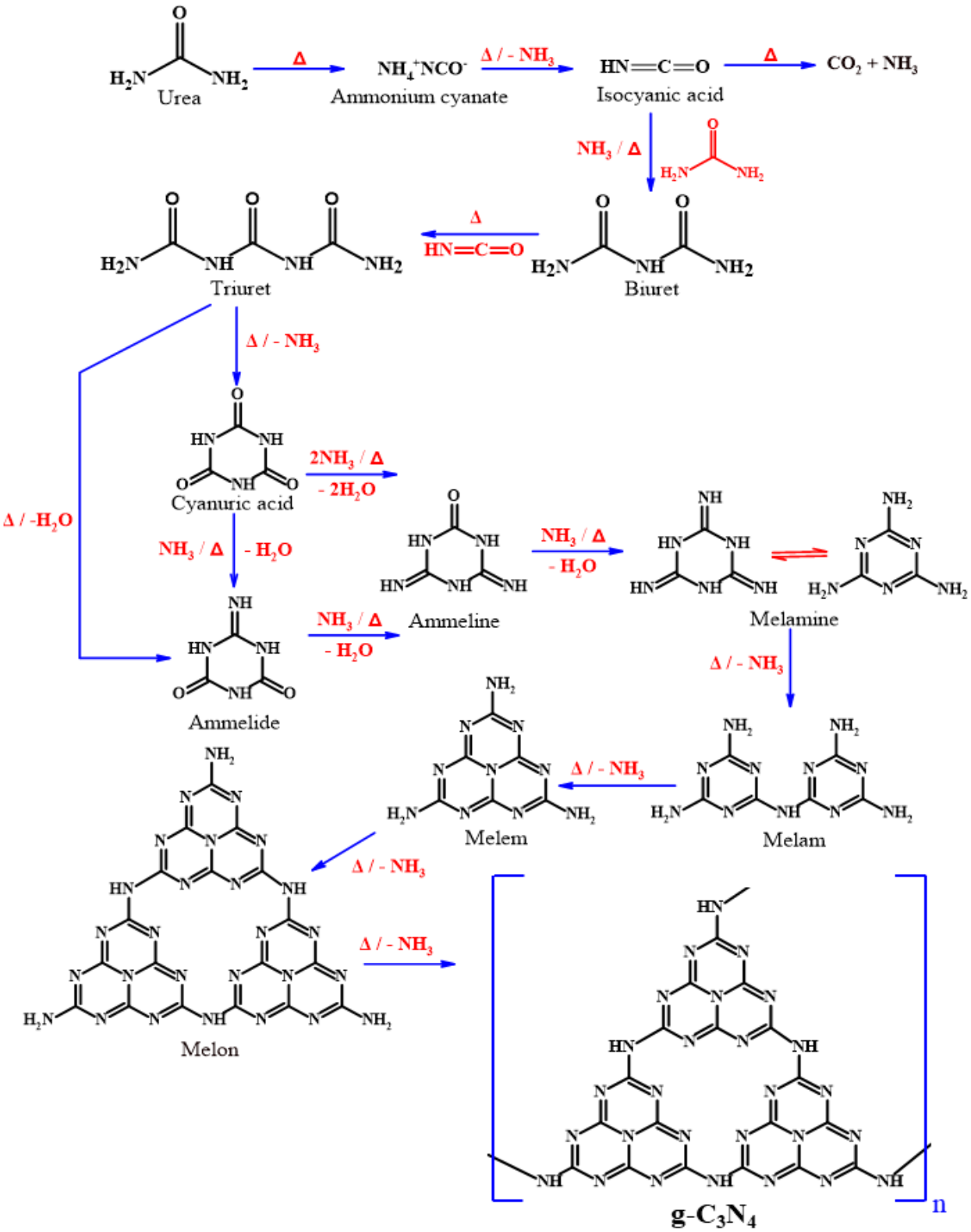

Scheme 1: *The sequence of reactions considered for the one-pot synthesis of g-C_3N_4 through urea pyrolysis. The ammonia produced during different reaction steps further take part in the reaction sequence, thereby making the process self-supported. Note that, the sequence presented above does not contain the stoichiometry of respective reactions and also, reaction intermediated are not shown.*

The microscopic events as well as the hypothetical monolayer building steps related to Scheme 1 which have been considered for the KMC calculations (reaction label **1** to **22**), are reported in Table S1. Each event is characterized by a rate constant $k = k_O\, T^n e^{-E_a/k_B T}$ where k_0, T, E_a, and k_B stand for the pre-exponential factor, the temperature, the energy barrier, and the Boltzmann constant, respectively. For the reaction steps, the energy barriers are obtained through the optimization of the reactants, intermediates, products and the corresponding transition states, using density functional theory (DFT) calculations using the Gaussian09 package and at the B3LYP/6-31G+(d,p) level of theory, which has previously been shown to yield significantly accurate thermochemistry of carbon nitride materials.[43,50-52] The stability of the wave functions is confirmed for all the transition states. Harmonic frequency calculations are performed to ensure that the reactants and products are at the local minima while transition states (TS) are first order saddle points. The classical rate constants for over the barrier transformations are obtained using canonical variational transition state (CVT) theory.[53, 54]The corresponding zero-point energy corrected Gibbs free energy profiles at 298 K are shown in Figure 1(a-c) and all the quantum chemistry calculated kinetic data for the reactions are provided in Table 1.

As observed from Figure 1(a-c), first, urea and isocyanic acid combines to form biuret (event **1**) through **TS1,** having an activation energy of 19.5 kcal/mol, followed by the reaction between biuret and isocyanic acid to produce triuret (event **2, TS2**), the corresponding energy of activation being 24.5 kcal/mol. Triuret may undergo thermal cyclization to produce non-

aromatic tautomers of cyanuric acid **C1** (event **3, TS3**, Figure 1(a)) or ammelide **A1** (event **18**, **TS10,** Figure 1(b)), which yield NH_3 and H_2O, respectively. Both of the steps are associated with the highest energy barriers, i.e. 60.2 kcal/mol and 58.3 kcal/mol respectively (Figures 1(a) and 1(b)). Some of these transition states are shown in Figure 2(a) and the cartesian coordinates for all the TS's are reported in the supporting information file. The tautomers **C1** and **A1** may undergo conversion into the corresponding aromatic tautomeric forms **C4** and **A4** respectively through the intermediate tautomeric forms **C2**, **C3** (events **4** and **5,** Figure 2(b)) and **A2**, **A3** (events **19** and **20**), respectively. It is worthwhile to mention that, each step of the conversions of **C1→C2→C3→C4** (events **4** to **6** involving **TS4, TS5,** and **TS6** respectively) as well as **A1→A2→A3→A4** (events **19 to 21** involving **TS11, TS12,** and **TS13** respectively) are endergonic in nature, the non-aromatic tautomeric forms being thermodynamically more stable. The stability of the non-aromatic tautomeric forms may be attributed to the higher stability of the carbonyl bonds compared to the double bonds between carbon and nitrogen in the aromatic form. Only **A2** is observed to have quasi-identical stability with respect to **A1**, since both of the tautomers (aromatic and non-aromatic) contain a double bond between carbon and nitrogen, and the tautomeric equilibrium involves conversion of an exocyclic imine to an endocyclic one. However, as the non-aromatic molecules move towards the aromatic structures through several tautomeric steps, the energy of activation gradually decreases for both cyanuric acid and ammelide. Also, the energy barrier associated with each step of the multi-step conversion of triuret to cyanuric acid (Figure 1(a)) is higher compared to the analogous conversion of triuret to ammelide (Figure 1(b)) and therefore, it is expected that the reaction would preferentially go via the formation of ammelide, rather than involving cyanuric acid as an intermediate product. However, cyanuric acid (**C4**) can further be converted to ammelide by a reaction with water, going through **TS7** (event **7**). Once ammelide is formed, it reacts with ammonia and gets converted into ammeline (through **TS8,** event **8**) followed by another

reaction with ammonia molecule to produce melamine (through **TS9,** event **9**). On the other hand, urea molecules undergo thermal rearrangement via highly energetic **TS14** (the energy barrier being 47.1 kcal/mol) to generate ammonium cyanate (event **10**), which, further undergoes thermal expulsion of ammonia to produce isocyanic acid (event **11**), the latter being used for the reaction sequences given in Figure 1(a) and 1(b) for the production of biuret and triuret in consecutive reactions. Alternatively, isocyanic acid may react with water to produce the intermediate **Int1** (via **TS16**, event **12**), which, in turn, thermally decomposes via **TS17** into ammonia and carbon dioxide (event **13**), although the last reaction requires the climbing up of the huge energy barrier of 60.2 kcal/mol. After the formation of melamine, two units of melamine condenses through the release of ammonia to form melam (event **14**), which undergoes thermal rearrangement to produce melem (event **15**). In the KMC program, the melon grids are initiated by the condensation of two melem molecules to yield melon (event **16**). Now, the melon grid can be either extended through the successive addition of melem molecules (event **17**) or it undergoes condensation with another melon grid (event **22**) to produce a larger 2D grid structure of *g*-C_3N_4. Such a construction scheme yields planar graphitic carbon nitride sheets. Deifallah et al. showed that converged QM-calculated energy values can be obtained for such geometries, even if buckled-type conformations are expected.[55]

For the monomolecular reaction **11** of Table 1, k_0 is approximated using the TST ratio k_B/h, where h is the Planck constant, while as a realistic consideration, the rate constant of the monomolecular reaction **15** is chosen to be larger than the bimolecular reactions **14** and **16**. On the whole, each of the events belong to a propensity class characterized by a specific propensity formula (Table 2) and most of them are labelled using the equation number given in the reference 33.[33] Other events, such as reactions **16**, **17**, and **22**, labelled **Gs**, **Po**, and **Gm**, respectively, are involved in the growing of *g*-C_3N_4 monolayers. As already mentioned above, the reaction **16** involves the condensation of two melem molecules and initiates the building of

a grid for the further growing of a *g*-C_3N_4 sheet. In the process, a melem molecule is placed on a randomly selected lattice cell, in the direct vicinity of a central melem building block. Such a dimer lattice acts as a seed for reaction **17**, a polymerization-type reaction named **Po**, which corresponds to the addition of a melem building block to a randomly selected active lattice cell in a randomly selected grid. In the current version of the KMC program, reaction **17** occurs by adding the melem building block, either to a linear or non-linear melon grid. If the selected grid is linear, polymerization is forced to extend the linear structure, according to literature findings.[56-58] In the non-linear case, the monomer is added at a randomly selected active site of the already existing melon structure. The selection probability of an active site is either proportional, or inversely proportional, to the number of already occupied cells that surround the selected site. The first case corresponds to a situation where the probability for a melem molecule to react with a *g*-C_3N_4 lattice increases with the number of reaction sites n_{site}.

Table 1. *Quantum chemistry calculated kinetic data for the microscopic events implemented in the KMC code to model the synthesis of g-C_3N_4 monolayers. Reaction labels are in accordance with Table S1.*

Reaction label	**Elementary step**	k_0	n	E_a **(kcal/mol)**	**Propensity code**
1	urea + Isocyanic acid → biuret	2.0727×10^7	0	19.5	**2C**
2	Isocyanic acid + biuret → triuret	1.7044×10^8	0	24.5	**2C**
3	triuret →cyanuric acid tautomer (C1) + NH_3	5.3065×10^{10}	0	60.2	**2B**
4	cyanuric acid tautomer (C1)→ cyanuric acid tautomer (C2)	2.4376×10^{12}	0	45.8	**2B**
5	cyanuric acid tautomer (C2) → cyanuric acid tautomer (C3)	2.1833×10^{12}	0	42.0	**2B**

6	cyanuric acid tautomer (C3) →cyanuric acid tautomer (C4)	2.3232×10^{12}	0	36.4	**2B**
7	cyanuric acid tautomer (C4) + NH_3→ ammelide A4 + H_2O	2.0886×10^{8}	0	26.4	**2C**
8	ammelide + NH_3→ ammeline + H_2O	1.6729×10^{8}	0	38.6	**2C**
9	ammeline + NH_3→ melamine + H_2O	3.3481×10^{7}	0	47.6	**2C**
10	urea → ammonium cyanate	1.5202×10^{12}	0	47.1	**2B**
11	ammonium cyanate → Isocyanic acid + NH_3	2.084×10^{10}	1	40.1	**2B**
12	Isocyanic acid + H_2O → Int1	1.3905×10^{8}	0	16.3	**2C**
13	Int1 → NH_3 + CO_2	3.2709×10^{13}	0	60.2	**2B**
18	Triuret → ammelide tautomer (A1) + H_2O	5.4632×10^{10}	0	58.3	**2B**
19	ammelide tautomer (A1) → ammelide tautomer (A2)	3.6719×10^{12}	0	40.1	**2B**
20	ammelide tautomer (A2) → ammelide tautomer (A3)	2.0994×10^{13}	0	38.2	**2B**
21	ammelide tautomer (A3) → ammelide tautomer (A4)	1.3390×10^{12}	0	30.1	**2B**

Note: Units are s^{-1} for unimolecular reactions and $M^{-1}s^{-1}$ for bimolecular reactions. Except for **Gs**, **Po**, and **Gm** event types, the labels refer the equation numbers in reference 33, and the corresponding propensity formula are given in Table 2.

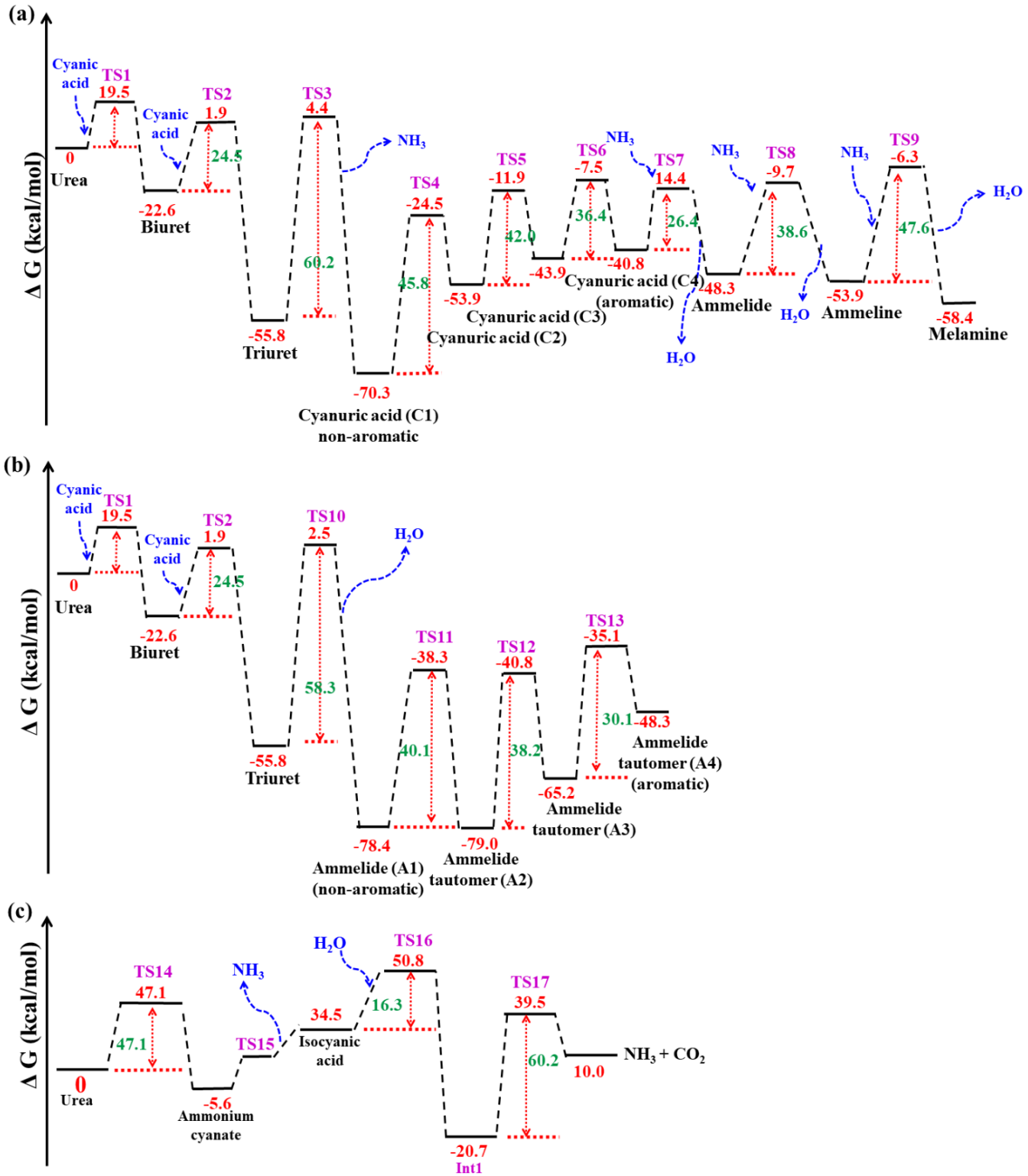

Figure 1: *Computed Gibbs free energy (zero-point energy corrected) diagram for (a) the stepwise self-supported reaction of urea to produce melamine, the precursor for g-C_3N_4, (b) alternative formation of ammelide from triuret, and (c) the conversion of urea into cyanic acid followed by decomposition.*

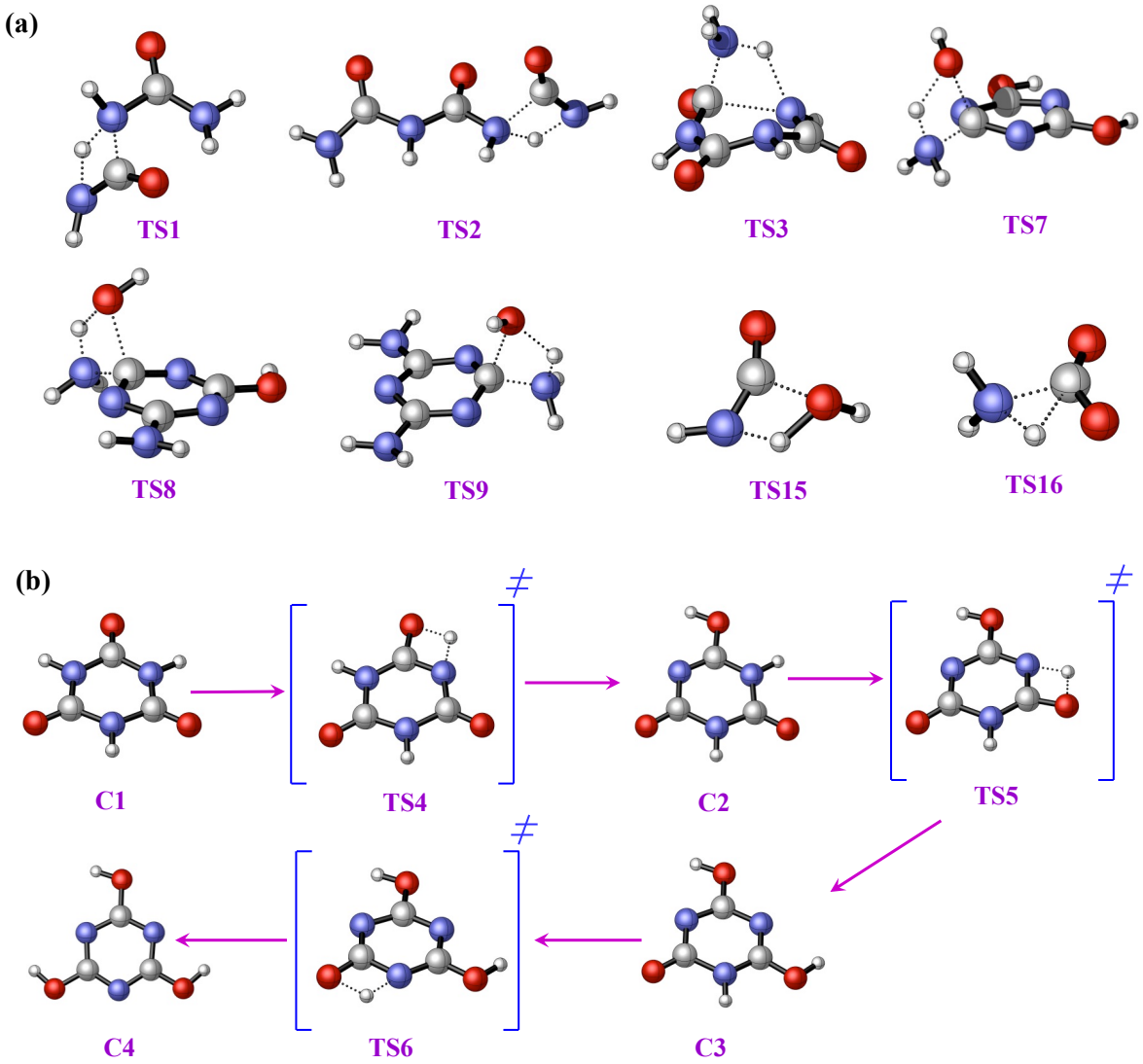

Figure 2: *DFT (B3LYP/6-31G+(d,p) level of theory) optimized structures of (a) selected transition states involved in the multistep pyrolytic conversion of urea into melamine and (b) the tautomeric aromatic and non-aromatic forms and the corresponding transition states involved in the tautomeric equilibrium of cyanuric acid. Oxygen atoms are depicted in red colour, nitrogen atoms in blue, carbon atoms in deep grey, and hydrogen atoms in steel.*

Table 2. *Classes of the events implemented in the KMC code.*

Propensity code	***Reaction type***	***Propensity formula***
2B	A → product(s)	$k\,[A]$
2C	A + B → product(s)	$k\,[A]\,[B]$
2D	2 A → product(s)	$k\,[A]\,([A]-1/N_aV)$

Gs	2 melem → melon grid seed	*k [monomer] ([monomer]-1/N_aV)*
Po	melem + melon grid	*k [monomer]*
Gm	Condensation of two melon grids	*k*

Note: N_a is the Avogadro number and V is the volume concerned.

Finally, it is considered that two melon grids can be condensed to larger g-C_3N_4 structures, as implemented in event **22** of type **Gm**. To take into account the relative mobility of the reactants, the rate constant of the bimolecular reactions of types **Po** and **Gm** are taken to be inversely proportional to the reduced mass μ, and increases (m = 1), or decreases (m = -1) with the number of possible melon reaction sites n_{site}, consistently with the selection mode of the active cell as described above (Table 2):

$$k = k_0 \, T^n \, n_{site}^m \, \mu^{-1/2} \, e^{-E_a/k_B T}$$

In the event type **Po**, n_{site} is calculated as the concentration of the active sites in the selected grid, while for the event type **Gm**, n_{site} is calculated as the product of the concentrations of the active sites in the first selected grid and active sites in the second selected grid. During the simulation, the propensity value of each event r, $p_r(t)$, varies with the number of molecules it involves, as shown in Table 2. Particularly, the total propensity value associated with an event of type **Po** is the summation of all propensity values of one grid, while the total propensity value associated with an event of type **Gm** is the summation of all propensity values involving both considered grids. Further technical details regarding the setup of the KMC simulations are mentioned in the supporting information file.

Several sets of calculation conditions were tested for the grid growing reaction (event **17**), which are summarized in Table S3. When the lattice cell selection and the rate constant associated with event **17** are directly proportional to the local number of reaction sites $\boldsymbol{n_{site}}$, the label ***"_dir"*** is used. In the opposite case, runs are named ***"_inv"***. The option ***"_dir"*** allows to avoid holes (unfilled lattice cells) inside a grid, while the option ***"_inv"*** is a way to extent the

size of an already existing grid. The growth of *g*-C_3N_4 sheets can be achieved by adding a melem molecule either to a linear or non-linear melon or grid structure. In the runs named ***"l_"***, linear structures are grown in a linear fashion only, while in runs named ***"nl_"***, the addition of a monomer to a linear structure is not necessarily achieved in a linear fashion. Particularly, in runs ***"l_"***, the growth of non-linear structures is achieved only through grid condensation (event **22**), i.e. the addition of a monomer to a non-linear grid is forbidden. On the other hand, in the runs named ***"lnl_"*** linear polymers are grown in a linear fashion, and non-linear grids are grown by adding one monomer at a time (Table S3). All calculations are allowed to run at 750 K, a temperature higher than the experimentally observed minimum reaction temperature so as to speed up the reaction steps. The propensity values for reactions **16**, **17**, and **22** were selected such that it allows the generation of a reasonable number of *g*-C_3N_4 lattices during the calculations. Indeed, the grid merge stage is highly time-consuming, which still needs to be optimised.

All calculations are run for 900,000 KMC steps, and the results are saved every 1,000 KMC iterations. The initial number of urea molecules, i.e., 375,940 in a volume of 5×10^{-20} L, is chosen so as to verify the density of liquid urea, i.e., 0.750 g/cm^3. The occurrence values of each event are reported in Table S4. The most frequent events are associated with the decomposition of urea, *i.e.*, events **1** and **10**, as well as to the consecutive reaction step **11**, regardless of the calculation options. In the frame of the selected run parameters, events **3** to **7** have almost identical statistical occurrence values due to similar propensity values, such as a lowering in the activation energy barrier is compensated by a lower pre-exponential factor. A similar behaviour is observed for the rearrangement process of ammelide in events **18** to **21**. After synthesis of biuret from urea (event **1**), the synthesis of ammelide preferentially occurs through reactions **2→18→19→20→21**, with ammelide **A1, A2, and A3** as the intermediate

products. The other reaction pathway, which involves events **3** to **7** with cyanuric acid **C1**, **C2**, and **C3** as the intermediate products, is far less frequent.

The main difference between the ***"_dir"*** and ***"_inv"*** KMC runs occurs at the level of the grid-building events, i.e., reactions **16**, **17**, and **22**. Indeed, using k_{17} values that are proportional to the number of local reaction sites leads to an increase in the frequency of events **16** and **22**, and to a decrease in the number of grid building steps (event **17**). Particularly, the number of occurrences of event **17** in the ***"_dir"*** and ***"_inv"*** conditions range between 1292 and 1535, and between 4736 and 5063, respectively (Table S4). Thus, in the ***"_inv"*** conditions, larger *g*-C_3N_4 lattices are expected due to numerous melem dimers which are less frequently used to build *g*-C_3N_4 grids, as illustrated later on. The evolution of the reactant and product profiles with time are displayed for the KMC calculations ***"lnl_dir"*** in Figure 3. It is worthwhile no mention that, the time scale has been normalized such that the total process time is set equal to unity.

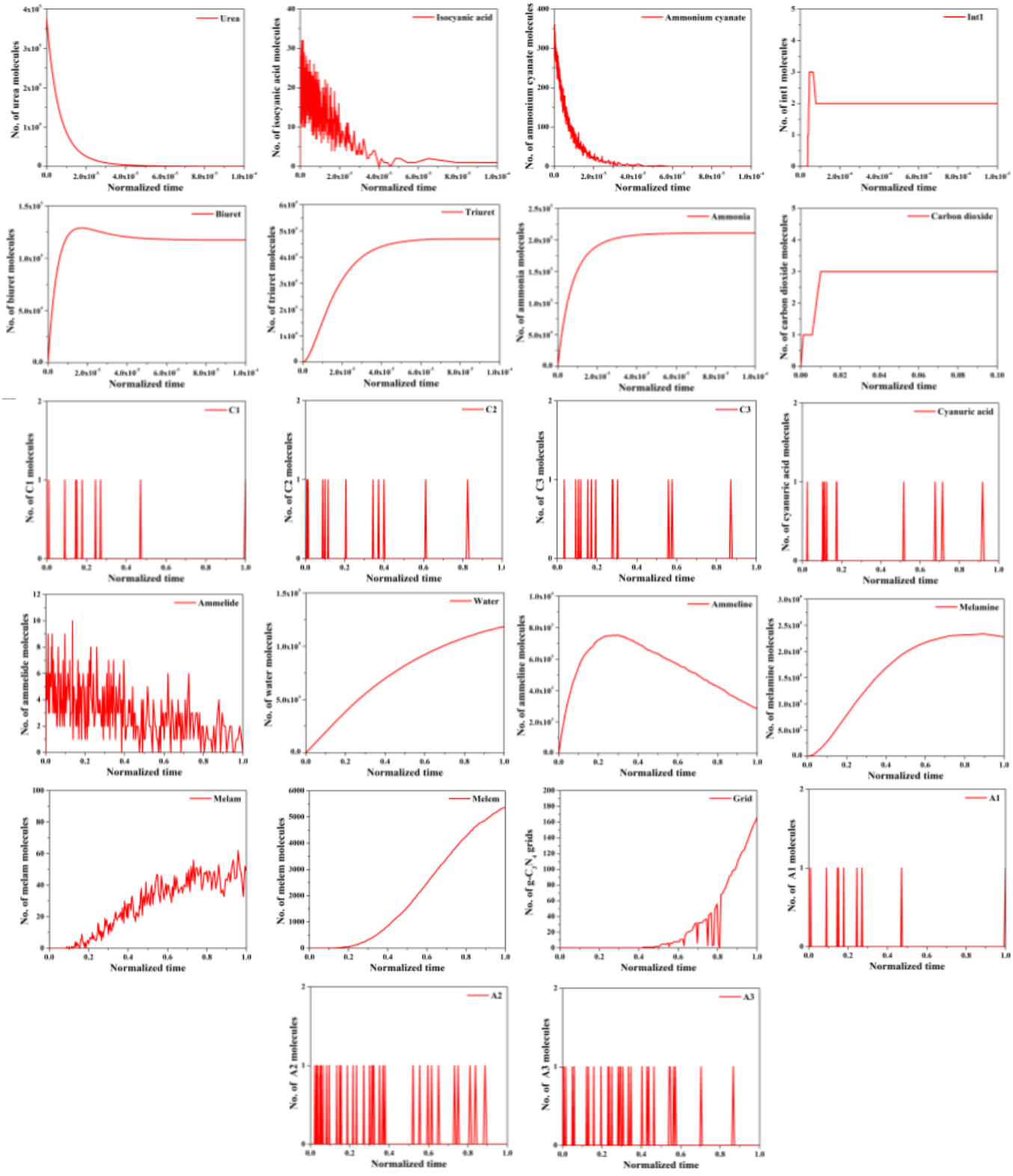

Figure 3. *Time dependent profiles of the number of reactant and product molecules as obtained from a single KMC run carried out with the option "**lnl_dir**" at 750 K.*

The profiles shown in Figure 3 illustrate that the number of urea molecules decreases very fast in the early stages of the KMC run, due to the initially large number of molecules. It

is only when the complete consumption of urea is observed, at a relative time of 8×10^{-5}, that ammeline, melamine, and water are produced. A high amount of urea prevents the synthesis of compounds leading to the apparition of melon and *g*-C_3N_4 structures. It is consistent with KMC results obtained with a constant urea concentration. In a such a particular case, the number of KMC steps and the values of k_{14} to k_{17} must be considerably increased to favour the apparition of *g*-C_3N_4 grids. Particularly, with a number of KMC steps = 40×10^6, with k_0 of events **14** and **16** = 5, and k_0 of events **15** and **17** = 100, one obtains 4 linear melon structures made of 16, 14, 3, and 3 melem moieties, and no *g*-C_3N_4 lattices, under the ***lnl_dir*** conditions.

The initial apparition of isocyanic acid is rapidly followed by a fast decrease, before a relative time of 0.0001. At that time, several compounds reach a stationary state, *i.e.*, biuret, triuret, and NH_3**,** while the low number of CO_2 adopts a stationary behaviour at larger times, slightly before t = 0.01. The amounts of other compounds progressively increase up to very large time scales, *e.g.*, H_2O, ammeline, melamine, melam, melem, and *g*-C_3N_4 grids. Particularly, the production of melam and melem is initiated at relative times of 0.09, right before the ammeline profile reaches a maximum at t = 0.27. The *g*-C_3N_4 profile strongly oscillates after the synthesis of the first grids around t = 0.42. It is due to the grid condensation phenomenon that is characterized by the merge of two grids into a single one. Some profiles, such as those of isocyanic acid, **C1** to **C3**, and **A1** to **A3** as well as ammelide (**A4**), lack smoothness, due to the low number of synthesized molecules. The profiles of the tautomer molecules **C1** to **C3** and **A1** to **A3** illustrate the lack of accumulation of these species during the run (Figure 3).

Similar to the occurrence frequency statistics (Table S4), the calculations show significant differences between the grids obtained with the two selected options ***"_dir"*** and ***"_inv"***. To illustrate such differences, statistics over different grid properties were calculated over 10 independent KMC runs (Figure S1 and Table 3). The grid size is defined as the number

of melem monomers in a lattice grid and the grid shape is calculated as the ratio of its two main inertia momenta I_{xx}/I_{yy}. The grid density is calculated as the grid mass (an integer number of the mass of the melem building block) divided by its 2D area. The statistical analysis of the *g*-C_3N_4 grids shows that large grids are favoured when k_{17} is inversely proportional to the number of local reaction sites, *i.e.*, with the option ***"_inv"***. As an example, average numbers of 5028 and 1659 melem building blocks are obtained with the options ***"lnl_dir"*** and ***"lnl_inv"***, respectively (Table 3). However, the grids are less numerous in the ***"_inv"*** case and are characterized by a lower surface density, i.e., 3.42 compared to 3.92 g/mol/A^2. A completely filled lattice is characterized by a maximal density value of 3.94 g/mol/A^2. Indeed, in the ***"_inv"*** case, the grids have a larger trend to extend their size at the expense of their density, so that they contain a larger number of holes. Particularly, the mean number of holes is equal to 5 and 458, for ***"lnl_dir"*** and ***"lnl_inv"***, respectively (Table 3).

Table 3. *Statistics (mean and standard deviation) over the g-C_3N_4 grids obtained for 10 KMC runs (Table S4). The labels "_dir" and "_inv" are used when the lattice cell selection and the rate constant associated with event **17** are directly and inversely proportional to the reaction sites.*

KMC options	***Total no. of grids***	***Grid Size (Max-min)***	***Grid Shape (Max-min)***	***Grid Density (Max-min)***	***No. of holes per grid (Max-min)***	***Hole size (Max-min)***
lnl_dir	18	**768 ± 687** (1659 – 3)	**6.6 ± 9.8** (42.0 – 1.3)	**3.92 ± 0.02** (3.85 – 3.94)	**5 ± 4** (15 – 1)	**1 ± 1** (7 - 1)
lnl_inv	10	**5028 ± 156** (5254 – 4774)	**1.2 ± 0.1** (1.5 – 1.1)	**3.42 ± 0.01** (3.44 – 3.41)	**458 ± 19** (487 – 425)	**2 ± 1** (19 - 1)
l_dir	14	**1132 ± 737** (2084 – 3)	**3.1 ± 3.0** (10.3 – 1.1)	**3.92 ± 0.01** (3.94 – 3.90)	**6 ± 4** (11 - 1)	**1 ± 1** (3 – 1)
l_inv	10	**5099 ± 143** (5249 – 4780)	**1.3 ± 0.2** (1.8 – 1.0)	**3.41 ± 0.1** (3.44 – 3.40)	**467 ± 16** (493 – 430)	**2 ± 1** (17 – 1)

nl_dir	23	**635 ± 720** (1739 – 3)	**3.4 ± 3.0** (10.3 – 1.0)	**3.93 ± 0.2** (3.94- 3.89)	**4 ± 4** (12 – 1)	**1 ± 1** (6 – 1)
nl_inv	10	**4790 ± 340** (5295 – 3952)	**1.3 ± 0.2** (1.7 – 1.0)	**3.41 ± 0.2** (3.45 – 3.38)	**430 ± 39** (485 – 344)	**2 ± 2** (29 – 1)

Due to the selected grid building approach, the defects in the *g*-C_3N_4 grids are of a single type, i.e., holes due to the absence of a one or several melem building blocks. Depending on the selected propensity calculation, i.e., either directly proportional (***_dir***) or inversely proportional (***_inv***) to the surrounding reactive sites (the number of neighbouring occupied cells), the holes are distributed along the grid borders or all over the *g*-C_3N_4 lattices, respectively. The largest grid obtained for each set of 10 KMC runs is displayed in Figure 4. In the ***"_inv"*** case, the largest holes are preferentially located at the periphery of the grids (Figure 4 (Right)).

It has been suggested by Thomas et al. that the passage of the melamine phase should be as rapid as possible so as to increase the mass efficiency in the polymerization process.[18] No kinetics data are available regarding the complexation of melamine with other species, but to reduce the life time of melamine, the value of k_{14} has been increased to the value of 5×10^{-6}. Similar to the calculations carried out with a rate constant of 5×10^{-7}, smaller and more numerous grids are obtained with the ***_dir*** simulation conditions. For all simulation conditions, the *g*-C_3N_4 grids are larger when $k_{14} = 5\times10^{-6}$ and lead to higher mass efficiency results which are about twice larger (Table S5). The results are also consistent with the observations reported by Alwin et al. who showed that using urea as the synthetic precursor yields lower mass efficiency values than using melamine.[59, 60] Indeed, when the synthesis of nitride graphite is directly simulated from melamine, only the grid-building events have non-zero propensity values. Thus, the KMC runs stops after a limited number of iterations due to a lack of reactants and the calculated mass efficiencies are larger, due to the fact that the products are *g*-C_3N_4 grids and NH_3 only. A mixture of urea and melamine can theoretically be considered as a precursor

which would combine the advantage of a cheap and less toxic reactant like urea with an increase in the propensities of the last synthetic steps. A KMC run carried out in the ***lnl_dir*** conditions, with 375,940 urea molecules and 10,000 melamine molecules showed a mass efficiency of 2.8% after 900,000 iterations, an intermediate value between 1.5 and 3.8% (Table S5).

Interestingly, the ratio of tertiary amine groups over the hydrogen bonded amine groups yields qualitative information about the size of the *g*-C_3N_4 sheets obtained during the KMC simulations. As experimentally studied by Thomas et al. through XPS measurements, such a ratio is linked to the degree of melon condensation.[18] In the current study, we have plotted the fraction n_3 of the N-R_3 moieties (which includes the tertiary amines and the central N atom of the heptazine cores), and the fraction n_{12} of the hydrogen-bonded amines, as a function of the distance from the centroid of the *g*-C_3N_4 grids (Figure S2). The distance at which both fractions coincide, i.e., when n_3/n_{12} reaches the value of 1, qualitatively corresponds to the mean radius of circular *g*-C_3N_4 sheets (Figure S2).

A plot of the hole size versus their shortest separation distance from the grid border is given in Figure 5, which illustrates the trend of large holes to be located close to the grid borders, while very small holes are distributed all over the grid surface. Ratios I_{xx}/I_{yy} close to unity characterize regular shapes. Besides the fact that the shape descriptor appears to be only slightly larger for the ***"_dir"*** runs, the grid shape seems to significantly differ for the runs ***"lnl_dir"***. Actually, the high values are due to small patterns, i.e., short linear grids composed of 3 to 6 monomers, and a slightly larger *g*-C_3N_4 lattice (Figure 6). On the whole, the most extended structures are obtained with the option ***"_dir"*** which favours the filling of grid holes rather than the condensation of melem molecules at the borders of a graphitic sheet (Figure S1). Holes remain rather small with mean values ranging from 1 to 2 empty lattice cells (Table

3). An investigation of the individual hole sizes shows that there is a trend for the holes to be larger with the ***"_inv"*** option (Table 3 and Figure 5).

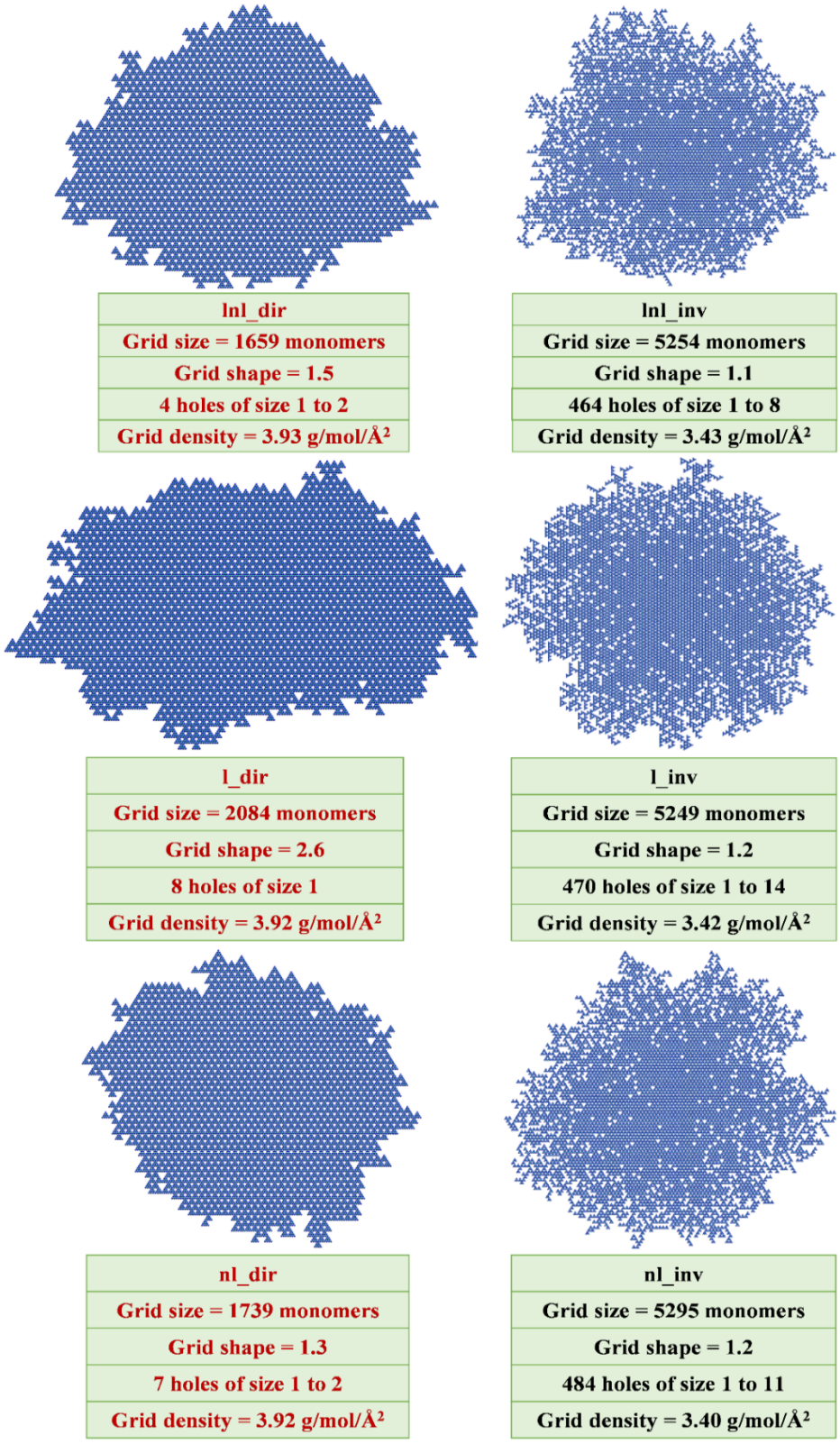

Figure 4. *Largest grids obtained from 10 KMC runs carried out with different simulation options at 750 K.*

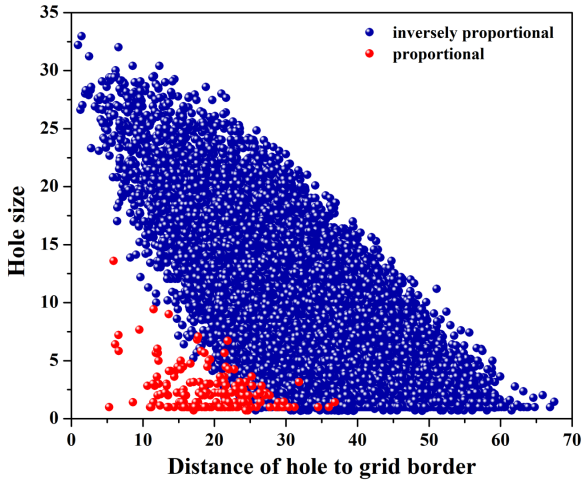

Figure 5. *Hole size versus hole distance from the grid border obtained using a cell filling propensity value that is proportional to (red) and inversely proportional to (blue) the number of surrounding reactive sites. Units are in cell numbers.*

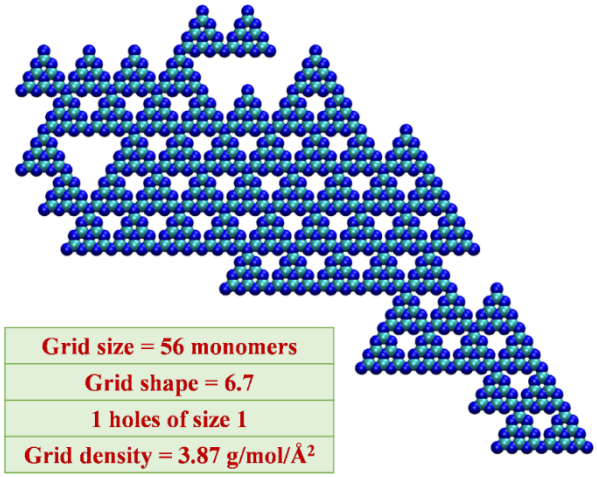

Figure 6. *Small g-C_3N_4 grid with large shape index obtained from a KMC run carried out with option* ***"lnl_dir"*** *at 750 K.*

In summary, the present article considers extensive electronic structure calculations to investigate the self-supported synthetic route for *g*-C_3N_4 and the quantum chemically determined rate constants are incorporated in a kinetic Monte-Carlo algorithm to simulate the synthesis of 2D *g*-C_3N_4 layers. For the end reaction steps, particularly those involving melon grid growing and condensation of melon grids, different calculation conditions were tested, *i.e.*, (i) the synthesis of *g*-C_3N_4 monolayers does require intermediate linear melon structures, or inversely, and (ii) the melem condensation stage is dependent, or inversely dependent, on

the number of local reaction sites of the monolayer. The examination of the grid patterns obtained under various calculation conditions sheds light into the understanding of experimental observations. High density grids are best obtained when the rate of the melem condensation stage is directly proportional to the number of local reaction sites of the monolayer. It is revealed that, larger holes (defects) appear near the grid borders while smaller holes tend to be present throughout the grid. The size of circular *g*-C_3N_4 sheets can be evaluated by the fractions of N-R_3 and hydrogen-bonded N atoms. Among the reaction steps that are considered in the present work, two different pathways allow to synthesize ammelide from urea. The KMC calculations showed that the pathway involving the direct conversion of biuret to a tautomer form of ammelide is favoured compared to the pathway involving cyanuric acid. On a futuristic note, various aspects of the KMC calculations could be considered in further studies such as reverse reactions, the consideration of the state of matter which might lead to additional phenomena such as diffusion. The calculation time of the KMC runs is mostly determined by the random selection events of grid reactive sites. Elaborate KMC calculations could include a revision of the current lattice-based approach implementation and its corresponding propensity values so as to adjust the simulated reaction times. It could involve a relaxation of the progressively synthesized g-C_3N_4 grids through, e.g., a molecular dynamics stage. We believe, the present work would provide significant "in-silico" evidence to understand the molecular events involved in the formation of g-C_3N_4 and allied nitrogen containing graphene-like 2D materials and simultaneously, enlighten experimentalists to control various facets of the synthetic protocols to produce such materials with specific physical properties e.g., shape, size and density.

AUTHOR INFORMATION

Corresponding Author

Corresponding Author: spad@iacs.res.in. Phone: +91-33-24734971.

ACKNOWLEDGMENT

TKM thanks CSIR for Senior Research Fellowship. AD acknowledges DST-Belspo program and SERB grant (CRG/2020/000301) for partial funding. LL carried out the research work in the frame of the Indo-Belgian Research and Technology Cooperation project BL/13/IN16 entitled "Optical Properties of MOFS/COFS". The present research also used resources of the 'Plateforme Technologique de Calcul Intensif (PTCI)' (http://www.ptci.unamur.be) located at the University of Namur, Belgium, which is supported by the FNRS-FRFC under the convention No. 2.5020.11. The PTCI is member of the 'Consortium des Équipements de Calcul Intensif (CÉCI)' (http://www.ceci-hpc.be).

Supporting Information

Microscopic events implemented in the KMC code to model the synthesis of *g*-C_3N_4 monolayers, unit cell coordinates of the melem building block, details regarding the KMC options of event 17, number of occurrences of each of the events as obtained from 10 KMC runs, distribution of the grid size, grid shape, grid density, number of holes, and size of holes, details of KMC simulations, co-ordinates for all transition states and complete reference of Gaussian 09.

References:

1. Ong, W.J.; Tan, L.L.; Ng, Y. H.; Yong, S.T.; Chai, S.P., Graphitic carbon nitride (g-C3N4)-based photocatalysts for artificial photosynthesis and environmental remediation: are we a step closer to achieving sustainability? *Chem. Rev.* **2016,** *116*, 7159-7329.

2. Zhao, Z.; Sun, Y.; Dong, F., Graphitic carbon nitride based nanocomposites: a review. *Nanoscale* **2015,** *7*, 15-37.

3. Lu, H.; Guo, Y.; Martin, J. W.; Kraft, M.; Robertson, J., Atomic structure and electronic structure of disordered graphitic carbon nitride. *Carbon* **2019,** *147*, 483-489.

4. Zhang, X.; Xie, X.; Wang, H.; Zhang, J.; Pan, B.; Xie, Y., Enhanced photoresponsive ultrathin graphitic-phase C3N4 nanosheets for bioimaging. *J. Am. Chem. Soc.* **2013,** *135*, 18-21.

5. Mamba, G.; Mishra, A. K., Graphitic carbon nitride (g-C3N4) nanocomposites: A new and exciting generation of visible light driven photocatalysts for environmental pollution remediation. *Appl. Catal. B* **2016,** *198*, 347-377.

6. Mukhopadhyay, T. K.; Datta, A., Delicate balance of non-covalent forces govern the biocompatibility of graphitic carbon nitride towards genetic materials. *ChemPhysChem* **2020,** *21,* 1836-1846.

7. Zheng, Y.; Lin, L.; Wang, B.; Wang, X., Graphitic carbon nitride polymers toward sustainable photoredox catalysis. *Angew. Chem. Int. Ed.* **2015,** *54*, 12868-12884.

8. Liu, Y.; Xie, D.; Song, M.; Jiang, L.; Fu, G.; Liu, L.; Li, J., Water desalination across multilayer graphitic carbon nitride membrane: Insights from non-equilibrium molecular dynamics simulations. *Carbon* **2018,** *140*, 131-138.

9. Safaei, J.; Mohamed, N. A.; Mohamad Noh, M. F.; Soh, M. F.; Ludin, N. A.; Ibrahim, M. A.; Roslam Wan Isahak, W. N.; Mat Teridi, M. A., Graphitic carbon nitride (g-C3N4) electrodes for energy conversion and storage: a review on photoelectrochemical water splitting, solar cells and supercapacitors. *J. Mater. Chem. A* **2018,** *6*, 22346-22380.

10. Xavier, M. M.; Nair, P. R.; Mathew, S., Emerging trends in sensors based on carbon nitride materials. *Analyst* **2019,** *144*, 1475-1491.

11. Zhou, Z.; Zhang, Y.; Shen, Y.; Liu, S.; Zhang, Y., Molecular engineering of polymeric carbon nitride: advancing applications from photocatalysis to biosensing and more. *Chem. Soc. Rev.* **2018,** *47*, 2298-2321.

12. Dong, Y.; Wang, Q.; Wu, H.; Chen, Y.; Lu, C.-H.; Chi, Y.; Yang, H.-H., Graphitic carbon nitride materials: sensing, imaging and therapy. *Small* **2016,** *12*, 5376-5393.

13. Goettmann, F.; Fischer, A.; Antonietti, M.; Thomas, A., Chemical synthesis of mesoporous carbon nitrides using hard templates and their use as a metal-free catalyst for Friedel–Crafts reaction of benzene. *Angew. Chem. Int. Ed.* **2006,** *45*, 4467-4471.

14. Groenewolt, M.; Antonietti, M., Synthesis of g-C3N4 nanoparticles in mesoporous silica host matrices. *Adv. Mater.* **2005,** *17*, 1789-1792.

15. Zhang, J.; Chen , X.; Takanabe, K.; Maeda, K.; Domen, K.; Epping, J. D.; Fu, X.; Antonietti, M.; Wang , X., Synthesis of a carbon nitride structure for visible-light catalysis by copolymerization. *Angew. Chem. Int. Ed.* **2010,** *49*, 441-444.

16. Yan, S. C.; Li, Z. S.; Zou, Z. G., Photodegradation performance of g-C3N4 fabricated by directly heating melamine. *Langmuir* **2009,** *25*, 10397-10401.

17. Lotsch, B. V.; Schnick, W., Thermal conversion of guanylurea dicyanamide into graphitic carbon nitride via prototype CNx precursors. *Chem. Mater.* **2005,** *17*, 3976-3982.

18. Thomas, A.; Fischer, A.; Goettmann, F.; Antonietti, M.; Müller, J.O.; Schlögl, R.; Carlsson, J. M., Graphitic carbon nitride materials: variation of structure and morphology and their use as metal-free catalysts. *J. Mater. Chem.* **2008,** *18*, 4893-4908.

19. Zhu, B.; Xia, P.; Ho, W.; Yu, J., Isoelectric point and adsorption activity of porous g-C3N4. *Appl. Surf. Sci.* **2015,** *344*, 188-195.

20. Bann, B.; Miller, S. A., Melamine and derivatives of melamine. *Chem. Rev.* **1958,** *58*, 131-172.

21. Schaber, P. M.; Colson, J.; Higgins, S.; Thielen, D.; Anspach, B.; Brauer, J., Thermal decomposition (pyrolysis) of urea in an open reaction vessel. *Thermochim. Acta* **2004,** *424*, 131-142.

22. Kurzer, F., Biuret and related compounds. *Chem. Rev.* **1956,** *56*, 95-197.

23. Mitoraj, D.; Kisch, H., The Nature of Nitrogen-modified titanium dioxide photocatalysts active in visible light. *Angew. Chem. Int. Ed.* **2008,** *47*, 9975-9978.

24. Zou, X.-X.; Li, G.-D.; Wang, Y.-N.; Zhao, J.; Yan, C.; Guo, M.-Y.; Li, L.; Chen, J.-S., Direct conversion of urea into graphitic carbon nitride over mesoporous TiO2 spheres under mild condition. *Chem. Commun.* **2011,** *47*, 1066-1068.

25. Guo, Q.; Xie, Y.; Wang, X.; Zhang, S.; Hou, T.; Lv, S., Synthesis of carbon nitride nanotubes with the C3N4 stoichiometry via a benzene-thermal process at low temperatures. *Chemical Communications* **2004,** 1, 26-27.

26. Bojdys, M. J.; Müller, J.-O.; Antonietti, M.; Thomas, A., Ionothermal Synthesis of crystalline, condensed, graphitic carbon nitride. *Chem. Eur. J.* **2008,** *14*, 8177-8182.

27. Khabashesku, V. N.; Zimmerman, J. L.; Margrave, J. L., Powder synthesis and characterization of amorphous carbon nitride. *Chem. Mater.* **2000,** *12*, 3264-3270.

28. Kim, M.; Hwang, S.; Yu, J.-S., Novel ordered nanoporous graphitic C3N4 as a support for Pt–Ru anode catalyst in direct methanol fuel cell. *J. Mater. Chem.* **2007,** *17*, 1656-1659.

29. Li, Y.; Zhang, J.; Wang, Q.; Jin, Y.; Huang, D.; Cui, Q.; Zou, G., Nitrogen-rich carbon nitride hollow vessels: synthesis, characterization, and their properties. *J. Phys. Chem. B* **2010,** *114*, 9429-9434.

30. Komatsu, T.; Nakamura, T., Polycondensation/pyrolysis of tris-s-triazine derivatives leading to graphite-like carbon nitrides. *J. Mater. Chem.* **2001,** *11*, 474-478.

31. Liu, J.; Zhang, T.; Wang, Z.; Dawson, G.; Chen, W., Simple pyrolysis of urea into graphitic carbon nitride with recyclable adsorption and photocatalytic activity. *J. Mater. Chem.* **2011,** *21*, 14398-14401.

32. Feng, D.; Cheng, Y.; He, J.; Zheng, L.; Shao, D.; Wang, W.; Wang, W.; Lu, F.; Dong, H.; Liu, H.; Zheng, R.; Liu, H., Enhanced photocatalytic activities of g-C3N4 with large specific surface area via a facile one-step synthesis process. *Carbon* **2017,** *125*, 454-463.
33. Gillespie, D. T. A general method for numerically simulating the stochastic time evolution of coupled chemical reactions. *J. Comput. Phys.* **1976,** *22*, 403-434.
34. Gillespie, D. T., Exact stochastic simulation of coupled chemical reactions. *J. Phys. Chem.* **1977,** *81*, 2340-2361.
35. Döntgen, M.; Schmalz, F.; Kopp, W. A.; Kröger, L. C.; Leonhard, K., Automated chemical kinetic modeling via hybrid reactive molecular dynamics and quantum chemistry simulations. *J. Chem. Inf. Model.* **2018,** *58*, 1343-1355.
36. Li, H.; Brédas, J.L., Kinetic Monte Carlo modeling of charge carriers in organic electronic devices: suppression of the self-interaction error. *J. Phys. Chem. Lett.* **2017,** *8*, 2507-2512.
37. Casalegno, M.; Raos, G.; Po, R., Methodological assessment of Kinetic Monte Carlo simulations of organic photovoltaic devices: the treatment of electrostatic interactions. *J. Chem. Phys.* **2010,** *132*, 094705.
38. Li, H.; Chavez, A. D.; Li, H.; Li, H.; Dichtel, W. R.; Bredas, J.-L., Nucleation and growth of covalent organic frameworks from solution: the example of COF-5. *J. Am. Chem. Soc.* **2017,** *139*, 16310-16318.
39. Zhang, X. Q.; Jansen, A. P. J., Kinetic Monte Carlo method for simulating reactions in solutions. *Phys. Rev. E* **2010,** *82*, 046704.
40. Piana, S.; Gale, J. D., Three-dimensional Kinetic Monte Carlo simulation of crystal growth from solution. *J. Cryst. Growth* **2006,** *294*, 46-52.
41. Zhu, Q.; Sharma, V.; Oganov, A. R.; Ramprasad, R., Predicting polymeric crystal structures by evolutionary algorithms. *J. Chem. Phys.* **2014,** *141*, 154102.
42. Rodgers, W. J.; May, P. W.; Allan, N. L.; Harvey, J. N., Three-dimensional kinetic Monte Carlo simulations of diamond chemical vapor deposition. *J. Chem. Phys.* **2015,** *142*, 214707.
43. Melissen, S. T. A. G.; Steinmann, S. N.; Le Bahers, T.; Sautet, P., DFT perspective on the thermochemistry of carbon nitride synthesis. *J. Phys. Chem. C* **2016,** *120*, 24542-24550.
44. Reshak, A. H., Thermoelectric properties for AA- and AB-stacking of a carbon nitride polymorph (C3N4). *RSC Adv.* **2014,** *4*, 63137-63142.
45. Gracia, J.; Kroll, P., Corrugated layered heptazine-based carbon nitride: the lowest energy modifications of C3N4 ground state. *J. Mater. Chem.* **2009,** *19*, 3013-3019.

46. Zuluaga, S.; Liu, L.H.; Shafiq, N.; Rupich, S. M.; Veyan, J.F.; Chabal, Y. J.; Thonhauser, T., Structural band-gap tuning in g-C3N4. *Phys. Chem. Chem. Phys.* **2015,** *17*, 957-962.

47. Jiang, L.; Yuan, X.; Pan, Y.; Liang, J.; Zeng, G.; Wu, Z.; Wang, H., Doping of graphitic carbon nitride for photocatalysis: A reveiw. *Appl. Catal. B* **2017,** *217*, 388-406.

48. Gao, G.; Jiao, Y.; Ma, F.; Jiao, Y.; Waclawik, E.; Du, A., Carbon nanodot decorated graphitic carbon nitride: new insights into the enhanced photocatalytic water splitting from ab initio studies. *Phys. Chem. Chem. Phys.* **2015,** *17*, 31140-31144.

49. Jing, B.; Ao, Z.; Teng, Z.; Wang, C.; Yi, J.; An, T., Density functional theory study on the effects of oxygen groups on band gap tuning of graphitic carbon nitrides for possible photocatalytic applications. *SM&T* **2018,** *16*, 12-22.

50. Lee, C.; Yang, W.; Parr, R. G., Development of the Colle-Salvetti correlation-energy formula into a functional of the electron density. *Phys. Rev. B* **1988,** *37*, 785-789.

51. Becke, A. D., A new mixing of Hartree–Fock and local density-functional theories. *J. Chem. Phys.* **1993,** *98*, 1372-1377.

52. Clark, T.; Chandrasekhar, J.; Spitznagel, G. W.; Schleyer, P. V. R., Efficient diffuse function-augmented basis sets for anion calculations. III. The 3-21+G basis set for first-row elements, Li–F. *J. Comput. Chem.* **1983,** *4*, 294-301.

53. Garrett, B. C.; Truhlar, D. G., Chapter 5 - Variational transition state theory. In *Theory and Applications of Computational Chemistry*, Dykstra, C. E.; Frenking, G.; Kim, K. S.; Scuseria, G. E., Eds. Elsevier: Amsterdam, 2005; pp 67-87.

54. Truhlar, D. G.; Garrett, B. C., Variational transition state theory. *Annu. Rev. Phys. Chem.* **1984,** *35*, 159-189.

55. Deifallah, M.; McMillan, P. F.; Corà, F., Electronic and structural properties of two-dimensional carbon nitride graphenes. *J. Phys. Chem. C* **2008,** *112*, 5447-5453.

56. Vidyasagar, D.; Ghugal, S. G.; Umare, S. S.; Banavoth, M., Extended π-conjugative n-p type homostructural graphitic carbon nitride for photodegradation and charge-storage applications. *Sci. Rep.* **2019,** *9*, 7186.

57. Zheng, Y.; Liu, J.; Liang, J.; Jaroniec, M.; Qiao, S. Z., Graphitic carbon nitride materials: controllable synthesis and applications in fuel cells and photocatalysis. *Energy Environ. Sci.* **2012,** *5*, 6717-6731.

58. Komatsu, T., The first synthesis and characterization of cyameluric high polymers. *Macromol. Chem. Phys.* **2001,** *202*, 19-25.

59. Zhang, W.; Zhang, Q.; Dong, F.; Zhao, Z., The multiple effects of precursors on the properties of polymeric carbon nitride. *Int. J. Photoenergy* **2013,** *2013*, 685038.
60. Alwin, E.; Kočí, K.; Wojcieszak, R.; Zieliński, M.; Edelmannová, M.; Pietrowski, M., Influence of high temperature synthesis on the structure of graphitic carbon nitride and its hydrogen generation ability. *Mater.* **2020,** *13*, 2756.

Supporting Information File

Molecular Mechanism for the Self-supported Synthesis of Graphitic Carbon Nitride from Urea Pyrolysis

Titas Kumar Mukhopadhyay[a], Laurence Leherte[b]*, Ayan Datta[a]*

[a]School of Chemical Sciences, Indian Association for the Cultivation of Science, 2A and 2B Raja S.C.Mullick Road, Jadavpur, Kolkata-700032, West Bengal, India.

[b]Unit of Theoretical and Structural Physical Chemistry, Namur Institute of Structured Matter (NISM), Namur Research Institute for Life Sciences (NARILIS), Namur Medicine & Drug Innovation Center (NAMEDIC), Department of Chemistry, Laboratory of Structural Biological Chemistry, University of Namur, Rue de Bruxelles 61, B-5000 Namur (Belgium)

Table of contents:

1. Events implemented in the KMC code:

Table S1. *Microscopic events implemented in the KMC code to model the synthesis of g-C_3N_4 monolayers*.

Label	Elementary step	k_0	n	E_a (kcal/mol)	Propensity code
1	urea + Isocyanic acid → biuret	2.0727×10^7	0	19.5	**2C**
2	Isocyanic acid + biuret → triuret	1.7044×10^8	0	24.5	**2C**
3	triuret →cyanuric acid tautomer (C1) + NH_3	5.3065×10^{10}	0	60.2	**2B**
4	cyanuric acid tautomer (C1)→ cyanuric acid tautomer (C2)	2.4376×10^{12}	0	45.8	**2B**
5	cyanuric acid tautomer (C2) → cyanuric acid tautomer (C3)	2.1833×10^{12}	0	42.0	**2B**
6	cyanuric acid tautomer (C3) →cyanuric acid tautomer (C4)	2.3232×10^{12}	0	36.4	**2B**
7	cyanuric acid tautomer (C4) + NH_3→ ammelide A4 + H_2O	2.0886×10^8	0	26.4	**2C**
8	ammelide + NH_3→ ammeline + H_2O	1.6729×10^8	0	38.6	**2C**
9	ammeline + NH_3→ melamine + H_2O	3.3481×10^7	0	47.6	**2C**
10	urea → ammonium cyanate	1.5202×10^{12}	0	47.1	**2B**
11	ammonium cyanate → Isocyanic acid + NH_3	2.084×10^{10}	1	40.1	**2B**
12	Isocyanic acid + H_2O → Int1	1.3905×10^8	0	16.3	**2C**
13	Int1 → NH_3 + CO_2	3.2709×10^{13}	0	60.2	**2B**
14	2 melamine → NH_3 + melam	5.0000×10^{-7}	0	0.0	**2D**
15	melam → NH_3 + melem	1.0000×10^{-4}	0	0.0	**2B**
16	Dimerization of melem → melon grid + NH_3	5.0000×10^{-7}	0	0.0	**Gs**
17	Grid growing of melon	1.0000×10^{-3}	0	0.0	**Po**

18	Triuret → ammelide tautomer (A1) + H_2O	5.4632×10^{10}	0	58.3	**2B**
19	ammelide tautomer (A1) → ammelide tautomer (A2)	3.6719×10^{12}	0	40.1	**2B**
20	ammelide tautomer (A2) → ammelide tautomer (A3)	2.0994×10^{13}	0	38.2	**2B**
21	ammelide tautomer (A3) → ammelide tautomer (A4)	1.3390×10^{12}	0	30.1	**2B**
22	Condensation of two melon grids	1.0000×10^{-1}	0	0.0	**Gm**

2. Unit cell coordinates of the melem building block:

Table S2. *Unit cell coordinates of the melem building block*

x	y	z	atomic weight
-0.642560	0.319751	0.000000	12.01
-0.423360	0.208178	0.000000	14.01
-0.311710	-0.014970	0.000000	12.01
-0.419260	-0.126540	0.000000	14.01
-0.638470	-0.014970	0.000000	12.01
-0.750120	0.208178	0.000000	14.01
-0.092510	-0.126540	0.000000	14.01
0.015035	-0.014970	0.000000	12.01
-0.096610	0.208178	0.000000	14.01
-0.315810	0.319751	0.000000	12.01

-0.427460	0.542897	0.000000	14.01
-0.646660	0.654470	0.000000	12.01
-0.754210	0.542897	0.000000	14.01
-0.744610	-0.125090	0.000000	14.01
-0.756874	0.874747	0.000000	14.01
0.231414	-0.125107	0.000000	14.01

3. Details regarding the KMC options of events 17:

Table S3. *Details regarding the KMC options of event 17*.

KMC run label	Linear polymers are grown in a linear fashion only one monomer at a time	Non-linear grids are grown one monomer at a time	Dependence of the propensity of event 17 with the no. of neighbouring filled lattice cells
lnl_dir	yes	yes	proportional
lnl_inv	yes	yes	inversely proportional
l_dir	yes	forbidden event	proportional
l_inv	yes	forbidden event	inversely proportional
nl_dir	no	yes	proportional
nl_inv	no	yes	inversely proportional

4. Occurrences of different events:

Table S4. *Number of occurrence (mean and standard deviation) of each event as obtained from 10 KMC runs. The KMC run options are explained in Table S3.*

Event	lnl_dir		lnl_inv		l_dir		l_inv		nl_dir		nl_inv	
index	mean	SD	mean	SD	mean	SD	mean	SD	mean	SD	mean	SD
1	164336.7	80.7	164378.9	97.5	164375.9	50.4	164356.7	91.2	164365.1	85.0	164359.3	85.6
2	47260.3	160.7	47176.3	194.6	47181.8	100.4	47219.0	182.7	47204.5	172.0	47215.4	171.6
3	8646.7	98.6	8571.5	88.9	8633.8	72.7	8561.6	95.1	8698.8	96.8	8569.5	65.7
4	8646.6	98.5	8571.5	88.9	8633.8	72.7	8561.5	95.0	8698.7	96.8	8569.5	65.7
5	8646.6	98.5	8571.5	88.9	8633.8	72.7	8561.5	95.0	8698.7	96.8	8569.5	65.7
6	8646.6	98.5	8571.5	88.9	8633.8	72.7	8561.5	95.0	8698.7	96.8	8569.5	65.7
7	8646.6	98.5	8571.4	88.8	8633.8	72.7	8561.5	95.0	8698.7	96.8	8569.5	65.7
8	40522.6	48.3	40087.2	23.9	40495.1	42.1	40082.6	42.1	40514.4	35.3	40127.2	39.9
9	37558.7	91.2	37089.2	63.7	37548.9	77.4	37048.5	106.2	37554.2	74.1	37090.0	71.7
10	211603.3	80.7	211561.1	97.5	211564.1	50.4	211583.3	91.2	211574.9	85.0	211580.7	85.6
11	211603.3	80.7	211561.1	97.5	211564.1	50.4	211583.3	91.2	211574.9	85.0	211580.7	85.6
12	6.3	3.1	5.9	2.3	6.4	3.1	7.6	2.3	5.3	2.9	6.0	2.0
13	6.3	3.1	5.9	2.3	6.4	3.1	7.6	2.3	5.3	2.9	6.0	2.0
14	7379.7	42.0	7054.9	84.5	7400.4	57.8	7023.0	96.7	7391.5	92.7	7037.0	77.5
15	7335.2	43.1	7011.2	86.3	7358.8	57.3	6980.4	98.2	7347.6	92.8	6995.2	80.1
16	176.5	12.2	78.1	10.8	173.1	17.5	74.2	8.0	194.1	12.5	92.8	14.1
17	1292.8	234.0	4988.2	166.3	1535.3	296.4	5063.0	153.2	1314.6	171.6	4736.0	368.5
18	31877.6	110.5	31517.0	101.5	31862.5	98.4	31522.7	117.6	31816.8	108.4	31558.8	67.2
19	31877.6	110.5	31516.9	101.6	31862.4	98.2	31522.5	117.5	31816.8	108.4	31558.5	67.6
20	31877.5	110.4	31516.8	101.6	31862.4	98.2	31522.4	117.4	31816.7	108.3	31558.4	67.6
21	31877.4	110.4	31516.8	101.6	31862.2	98.2	31522.4	117.4	31816.6	108.4	31558.3	67.4
22	175.1	12.4	77.1	10.8	171.2	17.3	73.2	8.0	193.1	11.9	92.2	14.1

5. Mass efficiency from KMC runs

Table S5. *Mass efficiency results (%) from single KMC runs under various simulation conditions*. n_{urea} *and* $n_{melamine}$ *stand for the initial numbers of molecules*.

KMC run label	**n_{urea} = 375,940** **$n_{melamine}$ = 0** **n_{KMC} = 900,000** **k_0 (event 14) = 5× 10^{-7}**	**n_{urea} = 375,940** **$n_{melamine}$ = 0** **n_{KMC} = 900,000** **k_0 (event 14) = 5× 10^{-6}**
lnl_dir	1.5	3.8
lnl_inv	4.9	10.3 [(a)]
l_dir	1.9	3.8
l_inv	4.9	10.0 [(a)]
nl_dir	1.5	4.0
nl_inv	4.9	9.7 [(a)]

[(a)] Estimated value: the *g*-C_3N_4 size reaches the limit of the pre-defined grid size.

6. Distribution of hole properties:

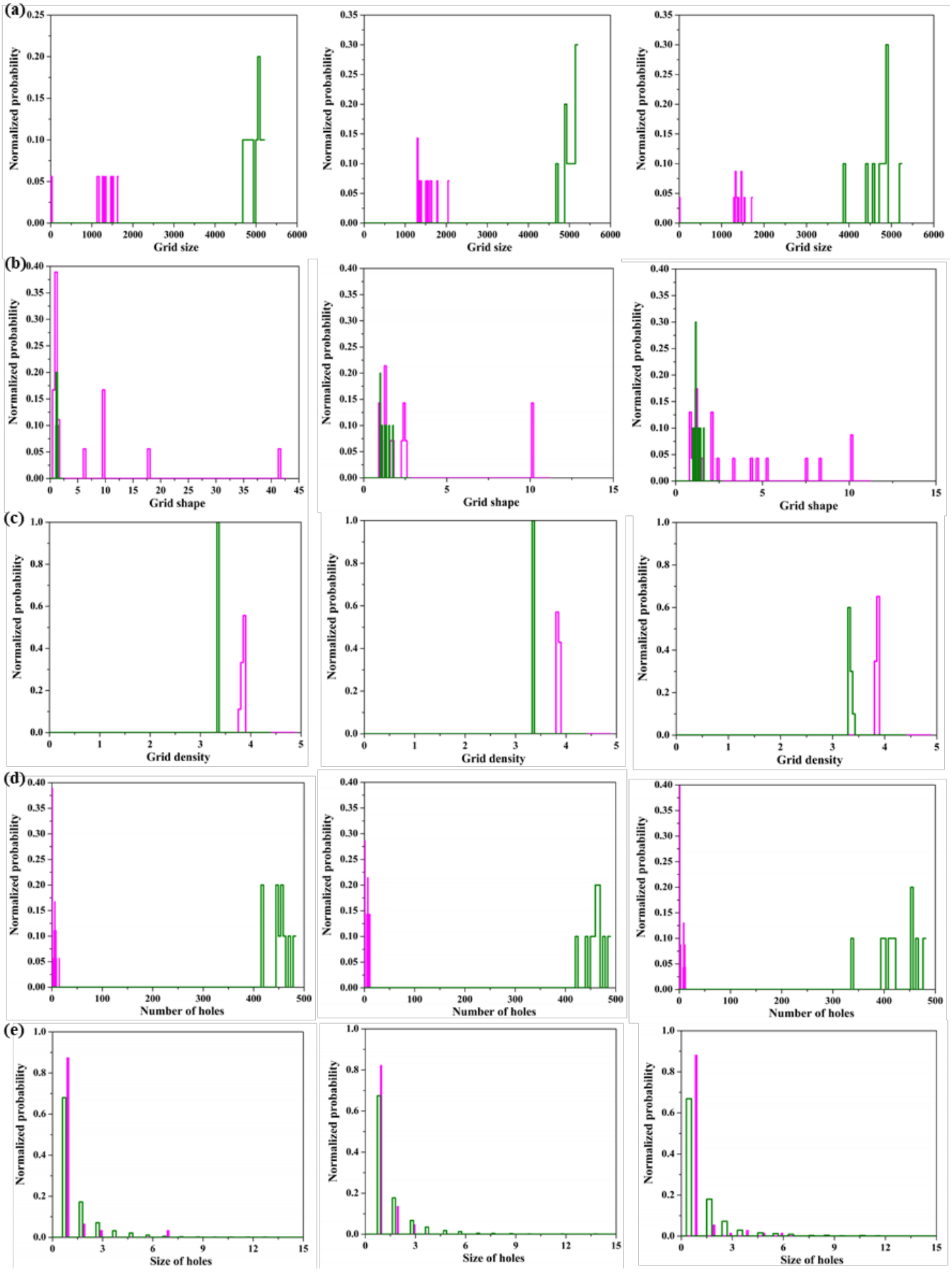

Figure S1. *Distribution of the (a) grid size, (b) grid shape, (c) grid density, (d) number of holes, and (e) size of holes as obtained from a statistical analysis of the grids generated through 10 independent KMC runs with the options* ***_dir*** *(magenta) and* ***_inv*** *(green). For each panel, the figures correspond to the KMC options* ***lnl_*** *(left),* ***l_*** *(middle) and* ***nl_*** *(right).*

7. Details of KMC simulations:

After reading the simulation conditions and event parameters, the initial propensity value of each event, $p_r(t)$, is calculated. The total propensity $P(0)$ is obtained as a summation over the individual values, $P(t) = \sum_{r=1}^{n_r} p_r(t)$, where n_r is the total number of event types. At each KMC iteration, a random number is selected between 0 and $P(t)$ from a uniform distribution to select an event. When the selected event is of type **Gs**, a dimer grid is created and is filled at its centre. If the event type is **Po**, a grid is randomly selected and an active cell is randomly selected for the addition of the monomer. The propensity of the active cell is directly or inversely proportional to its number of filled neighbouring cells. When the selected event is of type **Gm**, a Metropolis Monte Carlo (MMC) algorithm is used to select the binding mode of the two melon grids. During a given number of MMC iterations, superimpositions of the two randomly selected grids are generated. The superimposition with the maximal number of successful contacts (a successful contact occurs when an occupied cell of one grid is aligned with an active cell of the other grid) and no forbidden contacts (a forbidden contact occurs when two occupied cells are aligned) is chosen. If no successful condensation pattern is found during the given number of MMC steps, the event is invalidated, *i.e.*, no update occurs, and the KMC process goes on. For all events, the time is updated as $t+dt$ using a random number ξ, which implies that low total propensity values, *e.g.*, obtained at the end of a simulation, lead to high dt values where $dt = -\frac{\ln \xi}{P(t)}$. The numbers of molecules and the event propensity values are then updated. The whole process is repeated until the maximum number of iterations is

reached or when the total propensity is zero. In order to reduce the calculation time, only the event propensities that call for molecules involved in the reactive step are updated. The program thus involves an initial stage that looks for dependent reactions. The program ends with the building of the grid atom coordinates, the calculation of statistics, as well as the characterization of the grid holes using a floodfill-type algorithm. The building of the grid-based *g*-C_3N_4 atom coordinates is based on a crystal-type building block, with unit cell parameters a = 7.8875, b = 7.8875, c = 0.000 Å, α = 90.0, β = 90.0, γ = 60.0° (Table S2). The mass and area of that subunit are equal to 212.16 g/mol and 53.878 $Å^2$, respectively.

8. Profiles of the fraction of N atoms in the *g*-C_3N_4 sheets:

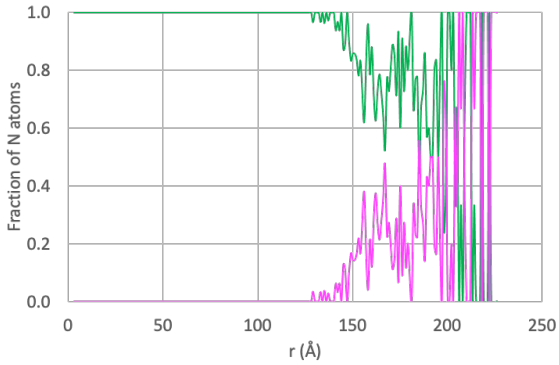

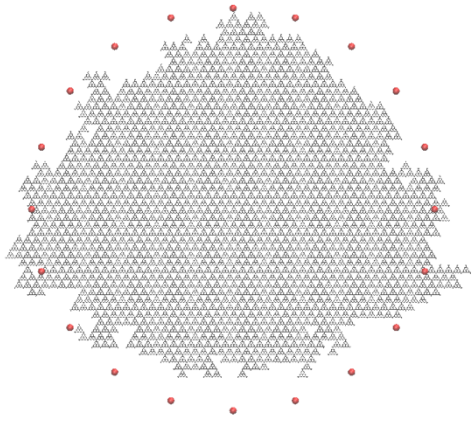

nln_dir **r = 185 Å**

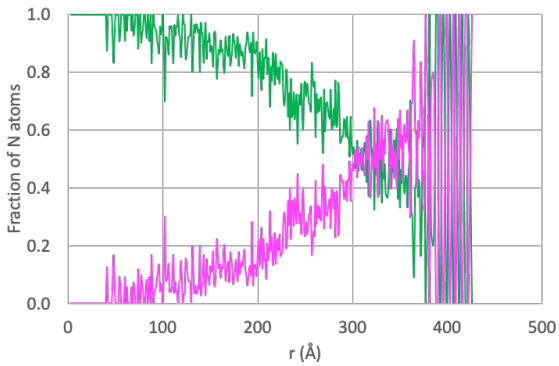

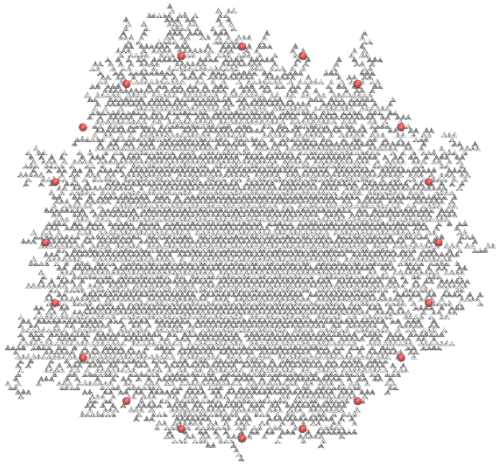

nln_inv

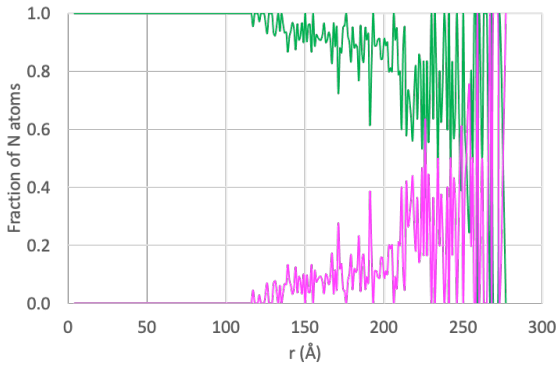

r = 302 Å

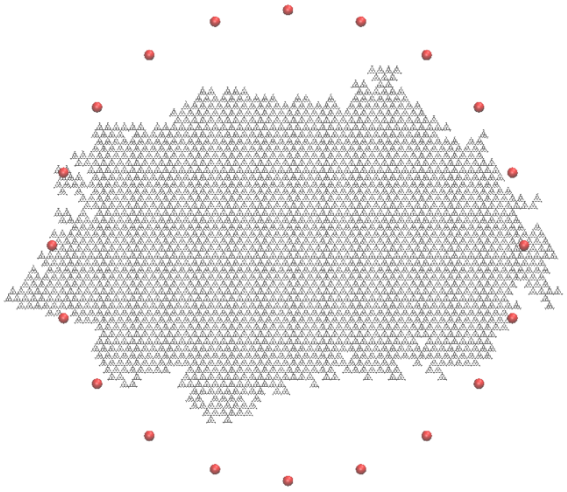

lin_dir

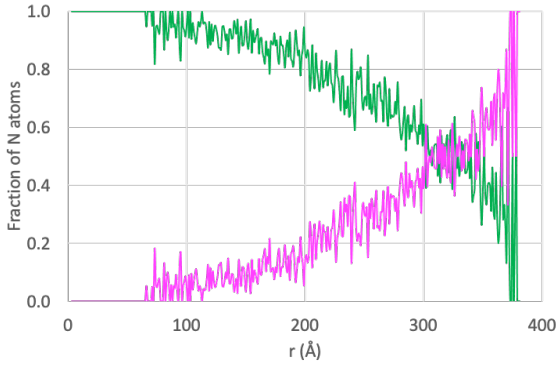

r = 226 Å

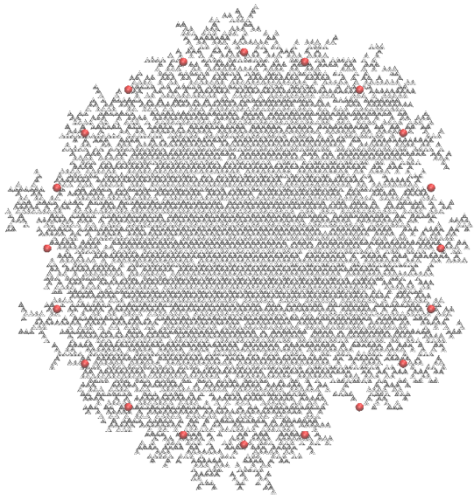

lin_inv

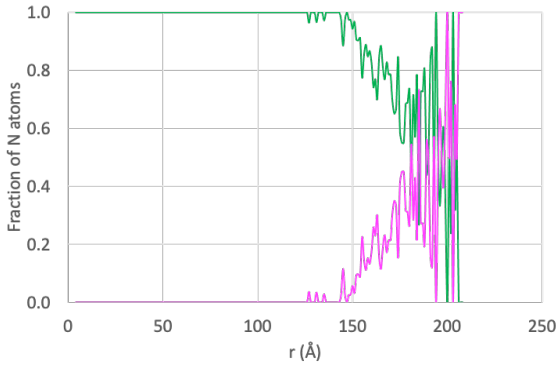

r = 301 Å

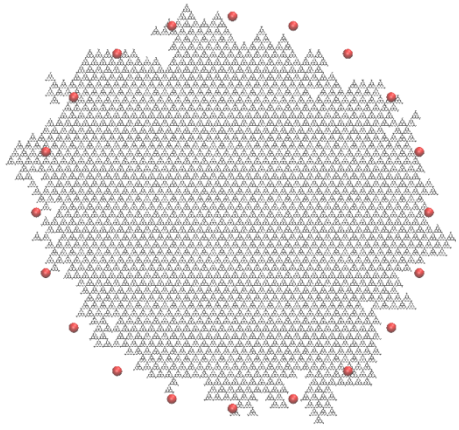

nolin_dir

r = 176 Å

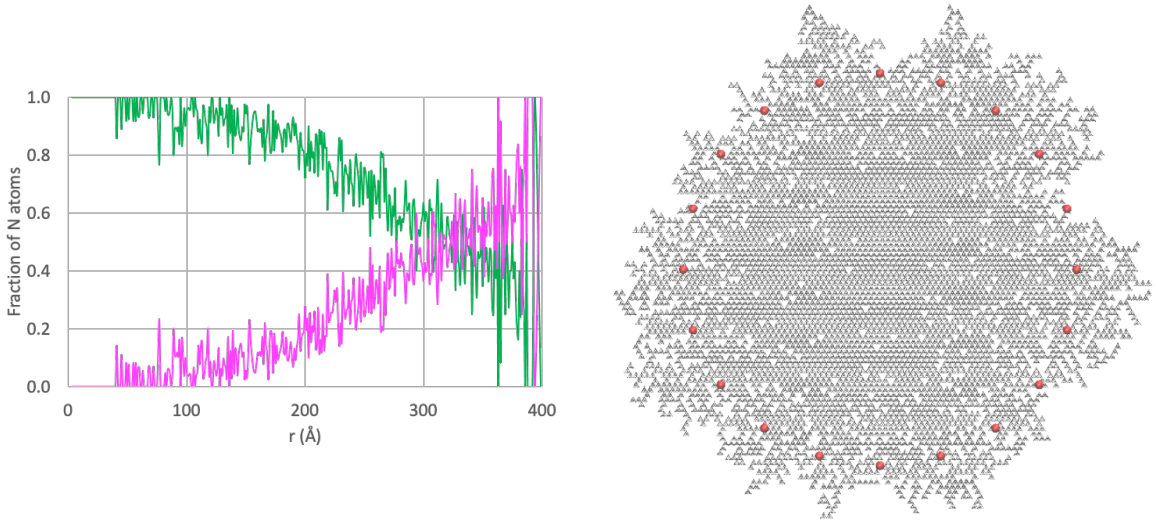

nolin_inv **r = 277 Å**

Figure S2. *(Left) Profiles of the fraction of tertiary N (n_3, green) and hydrogen-bonded amines (n_{12}, magenta) of the g-C_3N_4 structure displayed in Figure 4 of the paper. (Right) Structures as displayed in Figure 4 of the paper superimposed with red spheres delimiting a circle of radius r (r corresponds to the distance from the grid centroid at which the fractions of tertiary N and hydrogen-bonded amines are identical.*

9. Cartesian coordinates, energies and imaginary frequencies for the transition states:

Level of theory: B3LYP/6-31G+(d,p)

TS1

C	-0.15296400	0.77865200	0.60201200
O	0.56709700	0.45554700	-0.32354800
N	-1.02496700	-0.20860600	1.22254100
H	-0.69857000	-0.94455000	2.17751500
H	-1.46908000	-0.76141000	0.48764300
N	-0.21875900	1.99878100	1.18618800
H	-1.03457300	2.25529300	1.73192000
H	0.33053600	2.73068200	0.75973900
C	-2.00651000	0.16276100	2.42326800

N	-1.56569800	-0.78021600	3.23216600
O	-2.78138300	1.09908100	2.38740100
H	-1.97450100	-0.86692200	4.15800500

HF = -393.9264871 Hartree

Imaginary frequency = -1624.12 cm^{-1}

Temperature 298.150 Kelvin. Pressure 1.00000 Atm.

Zero-point correction=	0.085691 (Hartree/Particle)
Thermal correction to Energy=	0.092510
Thermal correction to Enthalpy=	0.093454
Thermal correction to Gibbs Free Energy=	0.054370
Sum of electronic and zero-point Energies=	-393.840796
Sum of electronic and thermal Energies=	-393.833978
Sum of electronic and thermal Enthalpies=	-393.833033
Sum of electronic and thermal Free Energies=	-393.872117

TS2

C	-1.62858700	-0.28154600	0.26701100
N	-0.55093900	-1.18737400	0.02969200
H	0.50942600	-0.77202700	-0.50027600
H	-0.81985100	-2.14594400	-0.18771300
N	-2.87752300	-0.81095600	-0.06579200
H	-2.91269000	-1.73124500	-0.48207900
C	-4.12848200	-0.20633400	0.22861700
N	-5.14975800	-0.76914100	-0.51789100
H	-6.04584100	-0.32203200	-0.37834000
H	-4.96411900	-1.07236100	-1.46414300
O	-1.43150400	0.83582000	0.67775300
O	-4.29507100	0.64156400	1.07553300
C	0.77489100	-1.16456500	1.18720900
N	1.60587200	-0.75425200	0.26085800
O	0.62451100	-1.49722000	2.32096200
H	2.57117400	-0.57785600	0.52525500

HF = - 562.6226835 Hartree

Imaginary frequency = -1635.21 cm^{-1}

Temperature 298.150 Kelvin. Pressure 1.00000 Atm.

Zero-point correction= 0.110934 (Hartree/Particle)

Thermal correction to Energy= 0.121442

Thermal correction to Enthalpy= 0.122386

Thermal correction to Gibbs Free Energy= 0.072979

Sum of electronic and zero-point Energies= -562.511750

Sum of electronic and thermal Energies= -562.501241

Sum of electronic and thermal Enthalpies= -562.500297

Sum of electronic and thermal Free Energies= -562.549704

TS3

C	1.32902900	-0.29832900	-0.46510600
N	1.09072300	1.06413100	-0.34315300
C	-0.06628700	1.76268000	0.05856000
N	-1.23497100	1.03525700	0.17029300
C	-1.66815500	-0.05012500	-0.70517400
O	2.17903100	-0.79833400	-1.16200900
O	0.01099600	2.95634500	0.30398300
O	-2.84049100	-0.03662300	-1.06761200
H	1.77692700	1.64741600	-0.80836900
H	-2.01298300	1.64464000	0.40407000
N	0.97954100	-1.08094100	0.84641900
H	1.68405700	-1.80917200	0.97342800
H	0.89179200	-0.49770400	1.68032500
N	-0.68914800	-0.94142800	-0.94062000
H	0.03525600	-1.44529600	0.47989300
H	-0.93493600	-1.55906400	-1.71113500

HF=-562.6419191 Hartree

Imaginary frequency = -473.91 cm^{-1}

Temperature 298.150 Kelvin. Pressure 1.00000 Atm.

Zero-point correction= 0.116288 (Hartree/Particle)

Thermal correction to Energy= 0.125221

Thermal correction to Enthalpy= 0.126165

Thermal correction to Gibbs Free Energy= 0.082143

Sum of electronic and zero-point Energies= -562.525631

Sum of electronic and thermal Energies= -562.516698

Sum of electronic and thermal Enthalpies= -562.515754

Sum of electronic and thermal Free Energies= -562.559776

TS4

C	0.10298000	1.15091800	-0.00069200
N	1.18213100	0.36278000	0.00093200
C	1.09469500	-1.01519800	0.00083000
C	-1.41020200	-0.71082600	-0.00043500
N	-1.16152000	0.68105400	-0.00097300
O	2.01801400	-1.79847800	0.00152800
O	0.50488700	2.36279200	-0.00076400
O	-2.53705900	-1.15908200	-0.00044000
N	-0.25471300	-1.46799400	-0.00013900
H	-1.96073000	1.30263300	-0.00164100
H	-0.38414000	-2.47284400	0.00077000
H	1.61267300	1.63441400	0.00109000

HF = -506.0838057 Hartree

Imaginary frequency = -1879.96 cm^{-1}

Temperature 298.150 Kelvin. Pressure 1.00000 Atm.

Zero-point correction= 0.074999 (Hartree/Particle)

Thermal correction to Energy= 0.081854

Thermal correction to Enthalpy= 0.082798

Thermal correction to Gibbs Free Energy= 0.043212

Sum of electronic and zero-point Energies= -506.008807

Sum of electronic and thermal Energies= -506.001952

Sum of electronic and thermal Enthalpies= -506.001008

Sum of electronic and thermal Free Energies= -506.040593

TS5

C	1.25037400	-0.12367100	-0.00062300
N	0.84930400	1.12367200	0.00077500
C	-0.49613200	1.41429900	0.00166500
C	-0.90384600	-0.97260300	-0.00037800
N	0.42712500	-1.19848900	-0.00126500
O	-0.98990700	2.52113000	0.00293500
O	2.55095100	-0.40248800	-0.00152800
O	-1.47760100	-2.11155100	-0.00110700
N	-1.39181200	0.26933600	0.00100100
H	-0.15590200	-2.38598900	-0.00204900
H	-2.38865100	0.45113400	0.00167400
H	3.02604100	0.44594400	-0.00095200

HF = -506.063707 Hartree

Imaginary frequency = -1855.97 cm^{-1}

Temperature 298.150 Kelvin. Pressure 1.00000 Atm.

Zero-point correction= 0.074749 (Hartree/Particle)

Thermal correction to Energy= 0.081509

Thermal correction to Enthalpy= 0.082453

Thermal correction to Gibbs Free Energy= 0.043128

Sum of electronic and zero-point Energies= -505.988958

Sum of electronic and thermal Energies= -505.982198

Sum of electronic and thermal Enthalpies= -505.981254

Sum of electronic and thermal Free Energies= -506.020579

TS6

C	0.99502600	-1.08290300	-0.00018300
N	1.38153200	0.20068500	-0.00024400
C	0.35330800	1.04874000	-0.00000500
C	-1.22141200	-0.65800200	0.00014700
N	-0.25442700	-1.57415800	-0.00014600
O	0.30692000	2.32370600	-0.00009800
O	1.95774500	-2.00247100	-0.00021800
O	-2.48987800	-1.05126700	0.00017400

N	-0.96963600	0.64659700	0.00032200
H	-1.00884100	1.92753300	0.00007700
H	2.80783100	-1.53135700	-0.00041300
H	-2.49381000	-2.02347200	0.00040300

HF = -506.0580107 Hartree

Imaginary frequency = -1846.19 cm^{-1}

Temperature 298.150 Kelvin. Pressure 1.00000 Atm.

Zero-point correction= 0.075185 (Hartree/Particle)

Thermal correction to Energy= 0.081788

Thermal correction to Enthalpy= 0.082732

Thermal correction to Gibbs Free Energy= 0.043816

Sum of electronic and zero-point Energies= -505.982825

Sum of electronic and thermal Energies= -505.976223

Sum of electronic and thermal Enthalpies= -505.975278

Sum of electronic and thermal Free Energies= -506.014195

TS7

C	1.17007600	0.10802800	-0.73548500
N	0.39413500	-1.00505000	-0.65045600
C	-0.79591500	-0.74815400	-0.13551900
C	-0.49147200	1.47722400	-0.18041000
N	0.71777600	1.38380900	-0.70231200
O	-1.59435900	-1.80706500	0.07538000
H	-2.43628900	-1.46415600	0.41453000
O	2.49297300	-0.04296500	0.58286100
H	2.28280800	-0.81427200	1.12980700
O	-0.97873200	2.71627200	-0.01926600
H	-1.87842400	2.62543300	0.33225800
N	-1.29575800	0.45915200	0.17449400
N	2.33597600	-0.06912800	-1.66316500
H	2.20139800	-0.87577100	-2.27200200
H	2.99090700	-0.23215100	-0.76133400
H	2.51339900	0.79041300	-2.18387100

HF = -562.6110903 Hartree

Imaginary frequency = -902.81 cm^{-1}

Temperature 298.150 Kelvin. Pressure 1.00000 Atm.

Zero-point correction= 0.114878 (Hartree/Particle)

Thermal correction to Energy= 0.123601

Thermal correction to Enthalpy= 0.124545

Thermal correction to Gibbs Free Energy= 0.081517

Sum of electronic and zero-point Energies= -562.496212

Sum of electronic and thermal Energies= -562.487489

Sum of electronic and thermal Enthalpies= -562.486545

Sum of electronic and thermal Free Energies= -562.529573

TS8

C	-1.38296200	-0.18165300	0.13609700
N	-0.73644700	-1.27938900	0.58693600
C	0.54044600	-1.32662200	0.22433900
C	0.50753200	0.73801800	-0.63358300
N	-0.83200400	0.82695400	-0.55318200
O	1.19826400	-2.45504800	0.55049600
H	2.11427800	-2.34261700	0.25230200
O	1.24156000	2.06837500	0.49637200
H	1.84925100	1.63700400	1.11362400
N	1.23119300	-0.39584800	-0.43645600
N	-2.72093600	-0.12983600	0.36242800
H	-3.19545600	0.74926700	0.23231200
H	-3.12185300	-0.82587000	0.97109200
N	1.08605500	1.61203400	-1.71544000
H	1.72305600	1.08452500	-2.31176900
H	1.56275400	2.25843700	-0.96266400
H	0.33546800	2.05690100	-2.24509900

HF = - 542.7497687 Hartree

Imaginary frequency = -716.39 cm^{-1}

Temperature 298.150 Kelvin. Pressure 1.00000 Atm.

Zero-point correction= 0.127228 (Hartree/Particle)

Thermal correction to Energy= 0.136532

Thermal correction to Enthalpy= 0.137476

Thermal correction to Gibbs Free Energy= 0.093440

Sum of electronic and zero-point Energies= -542.622541

Sum of electronic and thermal Energies= -542.613237

Sum of electronic and thermal Enthalpies= -542.612293

Sum of electronic and thermal Free Energies= -542.656329

TS9

C	0.38109500	0.91555000	-0.51587900
N	-0.95058400	0.71247800	-0.50325700
C	-1.28754600	-0.45952800	0.05148000
C	0.85185800	-1.17702700	0.12860400
N	1.33022200	-0.04298900	-0.40379500
O	0.76095700	2.24361400	0.79041500
H	1.43375900	1.87757500	1.38146400
N	-0.43421500	-1.42884500	0.43245000
N	-2.61856500	-0.71965500	0.19818800
H	-2.87092600	-1.52253400	0.75310300
H	-3.25055800	0.06522000	0.17053700
N	1.74237400	-2.18896900	0.34395600
H	2.72372300	-1.96054900	0.35157100
H	1.42251400	-2.97937300	0.88127800
N	0.78462900	2.01154300	-1.47267400
H	1.07875300	2.66955000	-0.65620600
H	-0.02810000	2.33038400	-2.00153100
H	1.54589400	1.70071400	-2.07584500

HF = - 522.8886569 Hartree

Imaginary frequency = -641.23 cm^{-1}

Temperature 298.150 Kelvin. Pressure 1.00000 Atm.

Zero-point correction= 0.139543 (Hartree/Particle)

Thermal correction to Energy= 0.149285

Thermal correction to Enthalpy= 0.150230

Thermal correction to Gibbs Free Energy= 0.105512

Sum of electronic and zero-point Energies= -522.749114

Sum of electronic and thermal Energies= -522.739371

Sum of electronic and thermal Enthalpies= -522.738427

Sum of electronic and thermal Free Energies= -522.783145

TS10

C	1.35092500	-0.43027600	-0.26352900
N	1.03913700	0.90776600	0.03542600
C	-0.11616600	1.41176100	0.56371900
N	-1.25084900	0.56966100	0.47675900
C	-1.35660600	-0.63562000	-0.15732400
O	1.36385600	-1.27875200	1.35386300
O	-0.22817500	2.53329600	1.02174900
O	-2.38935400	-1.18096200	-0.47620100
H	1.83802000	1.52838800	0.07439200
H	-2.12015200	1.01763600	0.74362000
N	2.33279600	-0.67816900	-1.03975400
H	2.52968300	-1.66525700	-1.17636600
N	-0.06979700	-1.26542800	-0.38256300
H	-0.09725200	-1.82954400	-1.23200600
H	2.25196000	-1.62593600	1.51701200
H	0.31100000	-1.79953400	0.52982200

HF = - 562.5975095 Hartree

Imaginary frequency = -865.06 cm^{-1}

Temperature 298.150 Kelvin. Pressure 1.00000 Atm.

Zero-point correction= 0.113194 (Hartree/Particle)

Thermal correction to Energy= 0.122289

Thermal correction to Enthalpy= 0.123234

Thermal correction to Gibbs Free Energy= 0.079035

Sum of electronic and zero-point Energies= -562.484315

Sum of electronic and thermal Energies= -562.475220

Sum of electronic and thermal Enthalpies= -562.474276

Sum of electronic and thermal Free Energies= -562.518475

TS11

C	0.63038800	1.37014900	-0.00618700
N	1.33242800	0.18627900	-0.00258500
C	0.80860600	-1.14292700	0.00338900
C	-1.32234400	-0.05195100	0.00144600
N	-0.76991200	1.19009900	-0.00413400
O	1.56021100	-2.09738200	0.00648900
O	1.12669200	2.47992400	-0.01079100
N	-0.55822600	-1.17165900	0.00484500
H	-1.32599100	2.03455800	-0.00648900
H	-1.81398100	-1.63949900	0.00830400
H	2.34199700	0.26434900	-0.00367000
N	-2.55496000	-0.49733400	0.00470500
H	-3.38885500	0.07538000	0.00328200

HF = - 486.200984 Hartree

Imaginary frequency = -1896.84 cm^{-1}

Temperature 298.150 Kelvin. Pressure 1.00000 Atm.

Zero-point correction= 0.086341 (Hartree/Particle)

Thermal correction to Energy= 0.093666

Thermal correction to Enthalpy= 0.094610

Thermal correction to Gibbs Free Energy= 0.054191

Sum of electronic and zero-point Energies= -486.114643

Sum of electronic and thermal Energies= -486.107318

Sum of electronic and thermal Enthalpies= -486.106374

Sum of electronic and thermal Free Energies= -486.146793

TS12

C	1.25037400	-0.12367100	-0.00062300
N	0.84930400	1.12367200	0.00077500
C	-0.49613200	1.41429900	0.00166500

C	-0.90384600	-0.97260300	-0.00037800
N	0.42712500	-1.19848900	-0.00126500
O	-0.98990700	2.52113000	0.00293500
O	2.55095100	-0.40248800	-0.00152800
O	-1.47760100	-2.11155100	-0.00110700
N	-1.39181200	0.26933600	0.00100100
H	-0.15590200	-2.38598900	-0.00204900
H	-2.38865100	0.45113400	0.00167400
H	3.02604100	0.44594400	-0.00095200

HF = - 506.063707 Hartree

Imaginary frequency = -1855.97 cm^{-1}

Temperature 298.150 Kelvin. Pressure 1.00000 Atm.

Zero-point correction= 0.086134 (Hartree/Particle)

Thermal correction to Energy= 0.093931

Thermal correction to Enthalpy= 0.094875

Thermal correction to Gibbs Free Energy= 0.052520

Sum of electronic and zero-point Energies= -486.117264

Sum of electronic and thermal Energies= -486.109468

Sum of electronic and thermal Enthalpies= -486.108524

Sum of electronic and thermal Free Energies= -486.150879

TS13

C	0.99502600	-1.08290300	-0.00018300
N	1.38153200	0.20068500	-0.00024400
C	0.35330800	1.04874000	-0.00000500
C	-1.22141200	-0.65800200	0.00014700
N	-0.25442700	-1.57415800	-0.00014600
O	0.30692000	2.32370600	-0.00009800
O	1.95774500	-2.00247100	-0.00021800
O	-2.48987800	-1.05126700	0.00017400
N	-0.96963600	0.64659700	0.00032200
H	-1.00884100	1.92753300	0.00007700
H	2.80783100	-1.53135700	-0.00041300

H	-2.49381000	-2.02347200	0.00040300

HF = -506.0580107 Hartree

Imaginary frequency = -1846.19 cm^{-1}

Temperature 298.150 Kelvin. Pressure 1.00000 Atm.

Zero-point correction= 0.075185 (Hartree/Particle)

Thermal correction to Energy= 0.081788

Thermal correction to Enthalpy= 0.082732

Thermal correction to Gibbs Free Energy= 0.043816

Sum of electronic and zero-point Energies= -505.982825

Sum of electronic and thermal Energies= -505.976223

Sum of electronic and thermal Enthalpies= -505.975278

Sum of electronic and thermal Free Energies= -506.014195

TS14

C	-0.12598600	-0.01403300	0.16953900
O	-0.30843800	1.12737800	0.53251100
N	-1.26560200	-1.11268600	0.08333200
H	-1.99864100	-0.87575100	-0.58363300
H	-1.68274800	-1.32644300	0.98810900
N	0.83865000	-0.82049900	-0.25421400
H	-0.20461600	-1.67909400	-0.29139700
H	1.78291400	-0.45774100	-0.33903100

HF= - 225.2119053 Hartree

Imaginary frequency = -1655.76 cm^{-1}

Temperature 298.150 Kelvin. Pressure 1.00000 Atm.

Zero-point correction= 0.058426 (Hartree/Particle)

Thermal correction to Energy= 0.062503

Thermal correction to Enthalpy= 0.063447

Thermal correction to Gibbs Free Energy= 0.032243

Sum of electronic and zero-point Energies= -225.153479

Sum of electronic and thermal Energies= -225.149402

Sum of electronic and thermal Enthalpies= -225.148458

Sum of electronic and thermal Free Energies= -225.179662

TS16

C	-2.60473400	1.79826200	-0.04248700
N	-3.26695400	0.68576700	-0.17765400
O	-2.51491000	2.97105500	-0.18038700
H	-4.22260700	0.70633800	-0.51477100
O	-1.31301100	0.90489500	0.70864900
H	-0.50196100	0.92368200	0.17596900
H	-2.20240600	0.15710700	0.35226100

HF = -245.0713466 Hartree

Imaginary frequency = -1625.17 cm^{-1}

Temperature 298.150 Kelvin. Pressure 1.00000 Atm.

Zero-point correction= 0.044469 (Hartree/Particle)

Thermal correction to Energy= 0.048631

Thermal correction to Enthalpy= 0.049575

Thermal correction to Gibbs Free Energy= 0.018174

Sum of electronic and zero-point Energies= -245.026877

Sum of electronic and thermal Energies= -245.022715

Sum of electronic and thermal Enthalpies= -245.021771

Sum of electronic and thermal Free Energies= -245.053173

TS17

C	-0.11057300	-0.02063400	0.04468700
N	-1.14954300	-1.17663200	-0.26450000
O	-0.39496400	1.12775100	0.23950200
H	-1.66573400	-1.04126000	-1.13325800
O	0.94855300	-0.75047200	-0.00440700
H	0.03553400	-1.63527200	-0.25105900
H	-1.80459600	-1.35228800	0.49678800

HF = - 245.0920591 Hartree

Imaginary frequency = -1706.69 cm^{-1}

Temperature 298.150 Kelvin. Pressure 1.00000 Atm.

Zero-point correction= 0.046402 (Hartree/Particle)

Thermal correction to Energy= 0.050294

Thermal correction to Enthalpy= 0.051238

Thermal correction to Gibbs Free Energy= 0.020292

Sum of electronic and zero-point Energies= -245.045657

Sum of electronic and thermal Energies= -245.041765

Sum of electronic and thermal Enthalpies= -245.040821

Sum of electronic and thermal Free Energies= -245.071767

10. Complete reference of Gaussian 09:

Frisch, M. J.; Trucks, G. W.; Schlegel, H. B.; Scuseria, G.E.; Robb, M. A.; Cheeseman, J. R.; Scalmani, G.; Barone, V.; Mennucci, B.; Petersson, G. A.; Nakatsuji, H.; Caricato, M.;Li, X.; Hratchian, H. P.; Izmaylov, A. F.; Bloino, J.; Zheng, G.; Sonnenberg, J. L.; Hada, M.; Ehara, M.; Toyota, K.;Fukuda, R.; Hasegawa, J.; Ishida, M.; Nakajima, T.; Honda, Y.; Kitao, O.; Nakai, H.; Vreven, T.; Montgomery, Jr., J. A.; Peralta, J. E.; Ogliaro, F.; Bearpark, M.; Heyd, J. J.; Brothers, E.; Kudin, K. N.; Staroverov, V. N.; Kobayashi, R.; Normand, J.; Raghavachari, K.; Rendell, A.; Burant, J. C.; Iyengar, S. S.; Tomasi, J.; Cossi, M.; Rega, N.; Millam, N. J.; Klene, M.; Knox, J. E.; Cross, J. B.; Bakken, V.; Adamo, C.; Jaramillo, J.; Gomperts, R.; Stratmann, R. E.; Yazyev, O.; Austin, A. J.; Cammi, R.; Pomelli, C.; Ochterski, J. W.; Martin, R. L.; Morokuma, K.; Zakrzewski, V. G.; Voth, G. A.; Salvador, P.; Dannenberg, J. J.; Dapprich, S.; Daniels, A. D.; Farkas, Ö.; Foresman, J. B.; Ortiz, J. V.; Cioslowski, J.; Fox, D. J. Gaussian 09, Gaussian, Inc., Wallingford CT, 2009.